



**HAL**  
open science

## Estimation of global black carbon direct radiative forcing and its uncertainty constrained by observations

Rong Wang, Yves Balkanski, Olivier Boucher, Philippe Ciais, Gregory L Schuster, Frédéric Chevallier, Bjørn Samset, Junfeng Liu, Shilong Piao, Myrto Valari, et al.

### ► To cite this version:

Rong Wang, Yves Balkanski, Olivier Boucher, Philippe Ciais, Gregory L Schuster, et al.. Estimation of global black carbon direct radiative forcing and its uncertainty constrained by observations. *Journal of Geophysical Research: Atmospheres*, 2016, 121 (10), pp.5948-5971. 10.1002/2015JD024326 . hal-02874050

**HAL Id: hal-02874050**

**<https://hal.science/hal-02874050>**

Submitted on 18 Jun 2020

**HAL** is a multi-disciplinary open access archive for the deposit and dissemination of scientific research documents, whether they are published or not. The documents may come from teaching and research institutions in France or abroad, or from public or private research centers.

L'archive ouverte pluridisciplinaire **HAL**, est destinée au dépôt et à la diffusion de documents scientifiques de niveau recherche, publiés ou non, émanant des établissements d'enseignement et de recherche français ou étrangers, des laboratoires publics ou privés.

## RESEARCH ARTICLE

10.1002/2015JD024326

## Key Points:

- A high-resolution inventory and nested model is used to estimate the radiation absorption by BC
- The underestimation in BC radiation absorption is reduced by 90% in Asia
- The BC RF is estimated to be  $0.53 \text{ W m}^{-2}$  with a range from 0.14 to  $1.19 \text{ W m}^{-2}$  by a Bayesian method

## Supporting Information:

- Supporting Information S1
- Data Set S1

## Correspondence to:

S. Tao,  
taos@pku.edu.cn

## Citation:

Wang, R., et al. (2016), Estimation of global black carbon direct radiative forcing and its uncertainty constrained by observations, *J. Geophys. Res. Atmos.*, 121, doi:10.1002/2015JD024326.

Received 9 OCT 2015

Accepted 10 MAY 2016

Accepted article online 13 MAY 2016

## Estimation of global black carbon direct radiative forcing and its uncertainty constrained by observations

Rong Wang<sup>1,2,3</sup>, Yves Balkanski<sup>2,3</sup>, Olivier Boucher<sup>4</sup>, Philippe Ciais<sup>2,3</sup>, Gregory L. Schuster<sup>5</sup>, Frédéric Chevallier<sup>2</sup>, Bjørn H. Samset<sup>6</sup>, Junfeng Liu<sup>1</sup>, Shilong Piao<sup>1,3</sup>, Myrto Valari<sup>7</sup>, and Shu Tao<sup>1,3</sup>

<sup>1</sup>Laboratory for Earth Surface Processes, College of Urban and Environmental Sciences, Peking University, Beijing, China, <sup>2</sup>Laboratoire des Sciences du Climat et de l'Environnement, CEA CNRS UVSQ, Gif-sur-Yvette, France, <sup>3</sup>Sino-French Institute for Earth System Science, College of Urban and Environmental Sciences, Peking University, Beijing, China, <sup>4</sup>Laboratoire de Météorologie Dynamique, IPSL/CNRS, Pierre et Marie Curie Université, Paris, France, <sup>5</sup>NASA Langley Research Center, Hampton, Virginia, USA, <sup>6</sup>CICERO Center for International Climate and Environmental Research, Blindern, Oslo, Norway, <sup>7</sup>Laboratoire de Météorologie Dynamique, IPSL/CNRS, Ecole Polytechnique, Palaiseau, France

**Abstract** Black carbon (BC) contributes to global warming by absorbing sunlight. However, the size of this contribution, namely, the direct radiative forcing (RF), ranges from  $+0.1$  to  $+1.0 \text{ W m}^{-2}$ , largely due to differences between bottom-up and observation-based estimates. Current global models systematically underestimate BC radiation absorption relative to observations, which is often attributed to the underestimation of BC emissions. Several studies that adjusted emissions to correct biases of global aerosol models resulted in a revised upward estimate of the BC RF. However, the BC RF was never optimized against observations in a rigorous mathematical manner. Here we simulated the absorption of solar radiation by BC from all sources at the 10 km resolution by combining a highly disaggregated emission inventory with a nested aerosol climate model and a downscaling method. As a result, the normalized mean bias in BC radiation absorption was reduced from  $-56\%$  to  $-5\%$  in Asia and from  $-71\%$  to  $-46\%$  elsewhere. We applied a Bayesian method that makes the best account of all model, representativeness, and observational uncertainties to estimate the BC RF and its uncertainty. Using the new emission inventory and high-resolution model reduces uncertainty in BC RF from  $-109\%/+172\%$  to  $-77\%/+78\%$  over Asia and from  $-83\%/+114\%$  to  $-64\%/+70\%$  over other continental regions. Finally, we derived an observationally constrained BC RF of  $0.53 \text{ W m}^{-2}$  (0.14 to 1.19 as 90% confidence) as our best estimate, less than previous estimates. Our estimate implies that reduction in BC emissions would contribute to slow down global warming, but the contribution could be less than previously thought.

### 1. Introduction

Burning fossil fuels, biofuels, and biomass not only produces carbon dioxide ( $\text{CO}_2$ ) but also smoke and soot. This emitted "black carbon" (BC) absorbs incoming solar radiation and contributes a net global warming effect [Ramanathan and Carmichael, 2008; Shindell et al., 2012; Bond et al., 2013; Boucher et al., 2013]. Previous estimates of the BC direct radiative forcing (RF) due to aerosol-radiation interaction (encompassing only the direct radiative forcing unless specified hereafter) have been derived either using a bottom-up approach with an atmospheric transport model fed with an emission inventory [Jacobson, 2001; Wang, 2004; Schulz et al., 2006; Kim et al., 2008; Ghan et al., 2012; Myhre et al., 2013a; Q. Q. Wang et al., 2014] or a top-down approach, in which atmospheric BC observations are used to constrain the model results [Sato et al., 2003; Chung et al., 2005, 2012; Ramanathan and Carmichael, 2008; Bond et al., 2013]. The majority of existing inventories estimate global BC emissions to be typically  $6\text{--}9 \text{ Tgyr}^{-1}$  [Bond et al., 2004, 2007, 2013; Dentener et al., 2006; Junker and Liousse, 2008; Lamarque et al., 2010; Granier et al., 2011; Jacobson, 2012; Q. Q. Wang et al., 2014], leading to a global BC RF of  $0.1\text{--}0.4 \text{ W m}^{-2}$  from the bottom-up approach [Schulz et al., 2006; Myhre et al., 2013a; Q. Q. Wang et al., 2014]. However, the same models that simulate radiation absorption by aerosols find that it is systematically underestimated by a factor of 2 to 6 relative to observations of aerosol absorption optical depth (AAOD) from the ground-based remote sensing Aerosol Robotic Network (AERONET) [Koch et al., 2009; Bond et al., 2013], leading to ad hoc adjustments in the so-called observation-based or top-down method. Previous studies chose to adjust the BC emissions upward to correct the low bias of global models, resulting in a larger revised BC RF [Sato et al., 2003; Chung et al., 2005, 2012; Ramanathan and Carmichael, 2008; Bond et al., 2013], in the range  $0.6\text{--}1.0 \text{ W m}^{-2}$ . This would make BC a

warming species as important as CH<sub>4</sub> according to the Fifth Assessment Report of the Intergovernmental Panel on Climate Change (IPCC) [Boucher *et al.*, 2013; Myhre *et al.*, 2013b].

Yet the uncertainty in BC RF is quite large. Recently, the RF of BC was estimated to be 0.71 W m<sup>-2</sup>, with a 90% confidence range of 0.08–1.27 W m<sup>-2</sup>, in an authoritative top-down multimodel study [Bond *et al.*, 2013]. However, large scaling factors are needed to adjust emissions in order to increase the simulated radiation absorption by BC for matching observations, similar to that in other observation-based studies [Sato *et al.*, 2003; Chung *et al.*, 2005, 2012; Ramanathan and Carmichael, 2008; Chung *et al.*, 2012]. As shown in the work by Bond *et al.* [2013], 11 of 17 models need a scaling factor larger than 2 to match the observed BC AAOD, while other models rely on high BC emissions (e.g., Goddard Institute for Space Studies (GISS)-general circulation model (GCM) II in Chung and Seinfeld [2002], Community Atmosphere Model (CAM3) ECA in Kim *et al.* [2008], MACR-Assim in Ramanathan and Carmichael [2008], and MACR in Chung *et al.* [2012]) or use aerosol schemes resulting in a long lifetime of BC of ~10 days (e.g., Spectral Radiation-Transport Model for Aerosol Species (SPRINTARS) in Schulz *et al.* [2006] and Gas, Aerosol, Transport, and Radiation air quality model (GATOR) in Jacobson [2010]). The reason for the large misfit of modeled to observed BC radiation absorption (AAOD) is yet not well understood. In contrast, observations of BC over the remote oceanic regions suggest that a short lifetime of BC is more reasonable [Kipling *et al.*, 2013; Q. Q. Wang *et al.*, 2014; Samset *et al.*, 2014; Hodnebrog *et al.*, 2014]. These uncertainties led to efforts to improve the physical treatment of BC in the model [Bauer *et al.*, 2010; Liu *et al.*, 2012; Jacobson, 2012; X. Wang *et al.*, 2014; Q. Q. Wang *et al.*, 2014]. However, X. Wang *et al.* [2014] found that after including the impact of brown carbon and considering the absorption enhancement due to BC coating, the BC AAOD is still underestimated in their model by a factor of 1.4–2.8 over different regions. In addition, when constraining model by observations, the uncertainties introduced by coarse-resolution models and spatial biases in the emission inventory were highlighted in many studies [Kim *et al.*, 2008; Koch *et al.*, 2009; Bauer *et al.*, 2010; Jacobson, 2012; Bond *et al.*, 2013], but their impact remains unknown. As a result, the observation-constrained estimate is very sensitive to uncertainties in observations and the simulated distribution of BC radiation absorption in space [Bond *et al.*, 2013]. Recently, Cohen and Wang [2014] applied a Kalman Filter approach to constrain the BC emission and revised BC emission upward to 17–18 Tg/yr; however, they did not estimate the subsequent BC RF. The uncertainty in the emission inventory was quantified in our recent studies [R. Wang *et al.*, 2014a, 2014b], while host model uncertainties of BC RF were quantified through AeroCom (Aerosol Comparisons between Observations and Models) experiments [Stier *et al.*, 2013]. An estimation of BC RF that makes the best account of all model, representativeness, and observational uncertainties is urgently needed to quantify the role of BC in climate change and its mitigation.

In this study, we use a recently developed emission inventory of BC combined with a nested aerosol climate model at high resolution over Asia to estimate the radiation absorption of BC globally. We evaluate the modeled BC AAOD at 900 nm using the AERONET retrievals. We consider all known uncertainties in the forward modeling of BC and retrieval of BC AAOD, and we also quantify for the first time the representativeness error that arises when comparing the simulated BC AAOD on a model grid to a point measurement. Finally, we apply a Bayesian method to obtain best estimates of BC radiation absorption and RF as well as their uncertainties.

## 2. Methodology

### 2.1. Retrieved BC Column Load and Radiation Absorption

We used retrievals from AERONET (Version 2.0 product) [Holben *et al.*, 1998; Dubovik and King, 2000] to evaluate our modeled BC AAOD. The AAOD at 900 nm was computed from the retrieved AERONET size distribution and refractive index. Missing refractive indices for low AOD values in Version 2.0 product were recovered from Version 1.5 product [Schuster *et al.*, 2009]. The BC AAOD at 900 nm was inferred from the AERONET retrievals by iterating the complex refractive index of a hypothetical internal mixture of BC, water, soluble aerosols, and insoluble mineral aerosols (dust) until a best fit is achieved with all of the AERONET real refractive indices, as well as the imaginary refractive indices at the 675, 870, and 1020 nm wavelengths using the Maxwell Garnett mixing rule [Schuster *et al.*, 2005, 2009]. This produced the volume fraction of BC, which was then multiplied by the retrieved column size distribution and a constant BC density (1.8 g cm<sup>-3</sup>) [Bond and Bergstrom, 2006] to obtain the BC column load.

Light-absorbing organic carbon (OC) is often referred to as “brown carbon” [Formenti *et al.*, 2003]; however, measurements show that light absorption by OC is close to zero at wavelengths longer than 650 nm

[Kirchstetter *et al.*, 2004]. Since OC does not absorb light in the 675–1020 nm wavelength range and we used only those wavelengths for the absorbing component of our retrievals, the presence of OC in the atmosphere does not affect the retrieved AAOD at 900 nm. Dust, however, may alter our retrievals in regions with heavy dust loading (e.g., West Africa). Thus, we accounted for the contribution of dust when retrieving the BC AAOD at 900 nm wavelength. We computed the optical properties of dust by treating dust as a mixture of quartz (78.5%), kaolinite (20.0%), goethite (1.3%), and hematite (0.2%). This mixture, namely, “*QKmix*,” predicts imaginary refractive index that achieves the best agreement with observations as shown by Schuster *et al.* [2012] or Kim *et al.*, [2011] (Figure S1 in the supporting information). Then, to test the influence of dust on the retrieved BC AAOD at 900 nm, we ran a sensitivity test at five representative AERONET sites (Bondville, Beijing, IER Cinzana, MCO-Hanimaadhoo, and Minsk) with different sets of dust optical properties, which correspond to the lower and upper bounds of light absorption by dust (Figure S1). In brief, we considered the upper bound of light absorption by dust by applying the optical properties of dust derived from the Optical Properties of Aerosols and Clouds database [Hess *et al.*, 1998], which predicts the highest imaginary refractive indices of dust (Figure S1). We considered the lower bound of light absorption by dust in a case without light absorption by this species. These tests resulted in a maximum discrepancy of  $\pm 18\%$  for the retrieved BC AAOD at 900 nm relative to that derived by using *QKmix* at the five representative AERONET sites (Figure S1b). Thus, we took  $\pm 18\%$  as the 90% uncertainty range to account for the error of the retrieved BC AAOD at 900 nm wavelength due to the variance in dust optical properties. In addition, we used a BC density of  $1.8 \text{ g cm}^{-3}$  in our retrieval as recommended by Bond and Bergstrom [2006]. Cohen and Wang [2014] found that their top-down estimate changes from  $-15\%$  to  $24\%$  when varying their baseline density ( $1.0 \text{ g cm}^{-3}$ ) by  $-16\%$  to  $+27\%$ . We followed Bond and Bergstrom [2006] and adopted a range of  $1.7\text{--}1.9 \text{ g cm}^{-3}$  for BC density (equivalent to an uncertainty of  $\pm 5\%$ ) as a 90% uncertainty range to account for the uncertainty in BC density.

There are two uncertainties that we cannot quantify for the retrieved AAOD at the present stage. Retrievals depend on aerosol shape and morphology but aerosols are only treated as either spheres or spheroids in current AERONET retrievals [Schuster *et al.*, 2016]. Second, retrievals can be unstable when using optical properties of an external mixture; thus, the internal mixture models are widely used [Dubovik and King, 2000], and the sensitivity of the retrievals to the aerosol state of mixture is unknown.

## 2.2. A new Global Emission Inventory of BC

A global  $0.1^\circ \times 0.1^\circ$  BC emission inventory PKU-BC-2007 ( $E_{\text{PKU}}$ ) [R. Wang *et al.*, 2014a] at the monthly resolution was developed for the year of 2007 based on a subnational fuel combustion data set [Wang *et al.*, 2013] and an updated data set of BC emission factors [R. Wang *et al.*, 2012a, 2012b, 2014a, 2014b]. A detailed description for the development of this inventory was summarized in R. Wang *et al.* [2014a]. A Monte Carlo approach was used to quantify the uncertainty associated with the emissions [R. Wang *et al.*, 2014a]. In brief, a 1000 point Monte Carlo run was performed by randomly drawing fuel consumption, BC emission factors, and technology fractions from given distributions in each run. Uniform probability distributions were applied for fuel consumption and technology fractions, while lognormal distributions from measurements were applied for the BC emission factors. As a result, we derived a distribution for the global total BC emission that is close to lognormal with a median of  $8.9 \text{ Tg yr}^{-1}$ , and 3.1, 5.4, 14.8, and  $32 \text{ Tg yr}^{-1}$  as the 5%, 25%, 75%, and 95% percentiles, respectively. Based on the Monte Carlo simulation, the three quartiles of the PKU-BC-2007 inventory were used to quantify the emissions (the second quartile) and the associated uncertainties (the first and third quartiles); all were used to run the two versions of Laboratoire de Météorologie Dynamique (LMDZ)-OR-Interaction with Chemistry and Aerosols (INCA) models to quantify the uncertainty.

## 2.3. Atmospheric Transport Models of BC

We used a global aerosol climate model LMDZ-OR-INCA [Schulz, 2007; Balkanski *et al.*, 2010; R. Wang *et al.*, 2014a; Hauglustaine *et al.*, 2014] to simulate the atmospheric transport, radiation absorption, and RF of BC. The model LMDZ-OR-INCA, couples online the LMDz (Laboratoire de Météorologie Dynamique, version 5) general circulation model [Hourdin *et al.*, 2006] and INCA (Interaction with Chemistry and Aerosols, version 4) an aerosol module [Schulz, 2007]. The interaction between the atmosphere and the land surface was accounted for by coupling LMDz with Organizing Carbon and Hydrology In Dynamic Ecosystems, version 9, a dynamical vegetation model [Krinner *et al.*, 2005]. We updated the optical properties of BC as described in section 2.4. In our study, two versions of LMDZ-OR-INCA working at different horizontal resolutions were

used, including one zoomed over Asia with a spatial resolution of  $0.51^\circ$  latitude by  $0.66^\circ$  longitude for a region ( $70^\circ\text{E}$ – $130^\circ\text{E}$ ,  $7^\circ\text{N}$ – $45^\circ\text{N}$ ) (a model run  $M_{\text{INz}}$ ) and another one with a fixed resolution of  $1.27^\circ$  latitude by  $2.50^\circ$  longitude globally (a model run  $M_{\text{IN}}$ ). The same vertical coordinate was used in the two versions with 19 layers from the surface to 4 hPa. In addition,  $M_{\text{IN}}$  and  $M_{\text{INz}}$  were run separately with identical treatments of size distributions, aerosol mixing state, sulphur chemistry, hygroscopic growth, removal processes, and radiative properties, which are all described in Schulz [2007] and Balkanski *et al.* [2010]. The grid systems in  $M_{\text{IN}}$  and  $M_{\text{INz}}$  are displayed in Figure S2. To run LMDZ-OR-INCA, the meteorological fields were nudged using the reanalyzed data produced by the European Centre for Medium-Range Weather Forecasts [European Centre for Medium-Range Weather Forecasts, 2003]. All simulations were run for the year of 2007 based on the  $E_{\text{PKU}}$  inventory [R. Wang *et al.*, 2014a] or the MACCity ( $E_{\text{MAC}}$ ), a reference inventory [Lamarque *et al.*, 2010; Granier *et al.*, 2011], taken for the same year (2007) with 3 months in 2006 as a spin-up. The emissions in  $E_{\text{PKU}}$  at a native resolution of  $0.1^\circ \times 0.1^\circ$  and  $E_{\text{MAC}}$  at a native resolution of  $0.5^\circ \times 0.5^\circ$  were both reprojected to the model resolutions of  $M_{\text{IN}}$  and  $M_{\text{INz}}$ . Therefore, a total of four combinations of BC emission inventory and transport model were considered and analyzed at global scale, that is,  $E_{\text{MAC}}/M_{\text{IN}}$ ,  $E_{\text{MAC}}/M_{\text{INz}}$ ,  $E_{\text{PKU}}/M_{\text{IN}}$ , and  $E_{\text{PKU}}/M_{\text{INz}}$ .

#### 2.4. Treatment of Aerosols in LMDZ-OR-INCA

The version of LMDZ-OR-INCA used in this study simulates BC, sulphate and associated ammonium, primary organic matter (POM), secondary organic matter, dust, and sea salt [Schulz, 2007; Balkanski *et al.*, 2010]. The emissions of POM and  $\text{SO}_2$  were taken from the AeroCom inventory for the year 2000 [Dentener *et al.*, 2006], while the secondary organic aerosol (with global total emission of  $19.1 \text{ Tg yr}^{-1}$ ) was included and treated as POM. Following a modal approach by Schulz *et al.* [1998], the aerosol size distribution is represented by multiple lognormal distributions in five different modes, namely, insoluble accumulation mode, soluble accumulation mode, coarse-insoluble mode, coarse-soluble mode, and supercoarse-soluble mode. The standard deviation of each lognormal size distribution was fixed, while the size distribution was tracked by using only two variables (the number and mass concentrations) in each mode. BC and POM were divided into hydrophobic (or insoluble) and hydrophilic (or soluble) parts. In LMDZ-OR-INCA, 80% of emitted BC/POM is assumed to be hydrophobic. The aging process then transfers hydrophobic BC/POM in the smaller size insoluble accumulation mode to hydrophilic BC/POM in the larger size-soluble accumulation mode. The lifetime of aging was taken as 1.6 days for BC/POM in the default version of LMDZ-OR-INCA according to Cooke and Wilson [1996].

In this study, we updated our model for aerosol optics. BC in the insoluble accumulation mode was computed using Mie calculations assuming a lognormal size distribution ( $r_0 = 0.0725 \mu\text{m}$ ,  $\sigma_g = 1.59$ ) of externally mixed particles [Schulz, 2007], a BC density of  $1.8 \text{ g/cm}^3$ , and a refractive index  $m = 1.95 - 0.79i$ . BC in the soluble accumulation mode was treated as an internal mixture considering insoluble BC inclusions in a soluble hygroscopic aerosol matrix. We used Mie calculations under the Maxwell Garnett mixing rule [Chýlek *et al.*, 1988], as derived originally by Maxwell Garnett [1904], to compute the equivalent refractive index ( $m_e$ ) of the soluble accumulation mode as

$$m_e^2 = m_0^2 \frac{m_A^2 + 2m_0^2 + 2v_A(m_A^2 - m_0^2)}{m_A^2 + 2m_0^2 - v_A(m_A^2 - m_0^2)} \quad (1)$$

where  $m_0$  is the refractive index of nonabsorbing soluble species, which is assumed to be that of a hygroscopic sulphate aerosol following Tang and Munkelwitz [1994];  $m_A$  is the refractive index of BC inclusions in the internal mixture; and  $v_A$  is the volume fraction of the BC inclusions in the soluble accumulation mode particle. Both  $v_A$  and  $m_0$  vary according to the simulated composition of the soluble accumulation mode and atmospheric relative humidity [Boucher, 2015], while we used the same density ( $1.8 \text{ g cm}^{-3}$ ) and refractive index as before for BC.

The size distribution for the dry aerosol is a lognormal with  $r_0$  of  $0.12 \mu\text{m}$  and  $\sigma_g$  of 1.59. We then computed the mass extinction cross section (MEC) and single-scattering albedo ( $\omega_0$ ) of the internal mixture. We attributed the absorption to the BC so that a mass absorption cross section (MAC) could be derived for BC ( $\text{MAC} = \text{MEC} \times (1 - \omega_0)$ ). The absorption enhancement ( $E_{\text{abs}} = \text{MAC}$  of internally mixed BC/MAC of externally mixed BC) as a function of the mass fraction of BC in the soluble accumulation mode ( $f_{\text{bc}}$ ) and the relative

**Table 1.** Comparison of the Global Average, Annual Mean RF of BC and Related Parameters in Our Model to Those From the AeroCom Phase I Experiments [Schulz et al., 2006]<sup>a</sup>

	$E$ (Tg yr <sup>-1</sup> )	$\tau$ (Day)	$L$ (mg m <sup>-2</sup> )	BC AAOD( $\times 1000$ )	BC RF (W m <sup>-2</sup> )	MAC (m <sup>2</sup> g <sup>-1</sup> )	MAC AIBCM (m <sup>2</sup> g <sup>-1</sup> )	MAC ASBCM (m <sup>2</sup> g <sup>-1</sup> )	AFE (W m <sup>-2</sup> AAOD <sup>-1</sup> )	NRFB (W g <sup>-1</sup> )
<i>Our Estimates</i>										
$E_{MAC}/M_{INz}$	6.0	5.9	0.20	1.89	0.30	9.5	5.5	10.2	159	1500
$E_{PKU}/M_{INz}$	7.5	5.5	0.23	2.14	0.34	9.3	5.5	10.0	159	1478
$E_{MAC}/M_{IN}$	6.0	6.7	0.24	2.20	0.35	9.2	5.5	9.9	159	1458
$E_{PKU}/M_{IN}$	7.5	6.1	0.29	2.52	0.40	8.7	5.5	9.7	159	1379
$E_{PKU}/M_{DS}$	7.5	5.9	0.27	2.45	0.39	9.1	5.5	9.9	159	1444
<i>AeroCom Phase I—Experiment B [Schulz et al., 2006]</i>										
GISS	4.9	7.2	0.24	1.83	0.22	8.4	-	-	120	920
LOA	4.9	7.3	0.25	1.98	0.32	8.0	-	-	162	1280
LSCE	4.9	7.5	0.25	1.11	0.30	4.4	-	-	270	1200
MPI-HAM	4.9	4.9	0.16	1.23	0.20	7.7	-	-	163	1250
SPRINTARS	4.9	10.6	0.37	3.50	0.32	9.8	-	-	91	860
UIO-CTM	4.9	5.5	0.19	1.34	0.22	7.2	-	-	164	1160
UIO-GCM	4.9	5.5	0.19	1.95	0.36	10.5	-	-	185	1890
UMI	4.9	5.8	0.19	1.29	0.25	6.8	-	-	194	1320
ULAQ	4.9	11.4	0.38	2.90	0.08	7.6	-	-	28	210
Mean	<b>4.9</b>	<b>7.3</b>	<b>0.25</b>	<b>1.90</b>	<b>0.25</b>	<b>7.8</b>	-	-	<b>153</b>	<b>1120</b>
Median	<b>4.9</b>	<b>7.2</b>	<b>0.24</b>	<b>1.83</b>	<b>0.25</b>	<b>7.7</b>	-	-	<b>163</b>	<b>1200</b>
SD	<b>0</b>	<b>2.3</b>	<b>0.08</b>	<b>0.82</b>	<b>0.08</b>	<b>1.8</b>	-	-	<b>68</b>	<b>450</b>

<sup>a</sup>BC emission ( $E$ ), BC lifetime ( $\tau$ ), BC column load ( $L$ ), BC AAOD (550 nm), BC RF, BC mass absorption cross section (MAC) at 550 nm, MAC of insoluble BC (AIBCM) at 550 nm, MAC of soluble BC (ASBCM) at 550 nm, absorption forcing efficiency (AFE) at 550 nm, and normalized RF of BC by BC burden (NRFB) are compared. BC emissions (including fossil fuel, biofuel, and outdoor biomass burning), column load, BC AAOD (550 nm), and RF are for industrial era BC as a difference between 1750 and 2007.

humidity is shown in Figure S3. The  $E_{abs}$  amounts to 1.6–2.2 at a wavelength of 550 nm, higher than the value (1.5) recommended by Bond et al. [2006] due to the difference in the two models. The  $E_{abs}$  decreases as  $f_{bc}$  increases as expected, while the  $E_{abs}$  decreases as RH increases despite the increased aerosol size because water scatters less light than sulphate in the mixture.

For computational reasons, we perform the Mie calculations off-line for a range of  $v_A$  and the relative humidity values using the globally averaged aerosol size distribution of the insoluble and soluble BC modes as derived from our global model. Then, we determine the optical properties of BC from a look-up table based on the humidity and  $v_A$  in each vertical layer at each time step in the global model. Results from sensitivity calculations show that this results in a very small error. The globally averaged MAC of insoluble BC, soluble BC, and total BC in LMDZ-OR-INCA are listed in Table 1.

Our model for aerosol optics does not take all types of coating into account. BC can be coated with material that is more or less hydrophilic. However, in the absence of good optical data on POM and secondary organic matter, we assumed that all coating material behaves like sulphate, and this limitation should be noted.

Aerosol morphology has also an impact on the BC optical properties. Adachi et al. [2010] estimated the optical properties and RF of BC based on a discrete dipole approximation method and the 3-D shapes of actual particles determined using electron tomography in Mexico City. They found that the bias in the global BC RF would be 6% using a Maxwell Garnett approximation and 24% using either a volume mixing or a core-shell model. However, the 3-D shapes of actual particles are only representative of one location, so we interpret this bias as an indication of the uncertainty rather than a systematic error that could be corrected for. We applied an additional uncertainty of 6% due to the mixing state and morphology of particles for our model calculations but not to the AERONET retrieval for which the uncertainty budget already accounts for uncertainties in the aerosol models. More measurements like Adachi et al. [2010] are necessary to better understand the uncertainty in global aerosol models.

At last, Oshima and Koike [2013] documented the limitation of using a constant lifetime for BC aging. Therefore, we implemented two new BC/POM aging schemes based on the work by Liu et al. [2012] and Zhang et al. [2015] which are discussed in section 4. It replaces the constant BC/POM aging rate with a varying aging rate that depends on the hydroxyl radical concentrations based on condensation and coagulation.

### 2.5. Interpolation of BC Column Load and Radiation Absorption to 10 km Resolution

Similar to an interpolation method applied in *R. Wang et al.* [2014a], the modeled BC loads were downscaled from the  $0.51^\circ \times 0.66^\circ$  grid ( $x,y$ ) in  $E_{PKU}/M_{INz}$  in Asia or the  $1.27^\circ \times 2.50^\circ$  grid ( $x,y$ ) in  $E_{PKU}/M_{IN}$  elsewhere to a  $0.1^\circ \times 0.1^\circ$  subgrid ( $i,j$ ) as

$$L_{i,j}^* = L_{x,y} \frac{E_{i,j}^\alpha}{\sum_{i,j} (A_{i,j} E_{i,j}^\alpha)} \quad (2)$$

where  $L_{i,j}^*$  is the downscaled BC load;  $L_{x,y}$  is the modeled BC load;  $E_{i,j}$  is the emission in the subgrid ( $i,j$ );  $\alpha$  is a seasonal-constant coefficient describing the nonlinear relationship between emission and column load; and  $A_{i,j}$  is the fractional area of each subgrid ( $i,j$ ) in the model grid ( $x,y$ ).

To optimize the values of  $\alpha$  in equation (2), a regional off-line chemistry-transport model CHIMERE ( $M_{CHIMERE}$ ) [Menut et al., 2013] was run with the  $E_{PKU}$  inventory over the North China Plain at a horizontal resolution of  $0.1^\circ \times 0.1^\circ$  (the same as  $E_{PKU}$ ) with eight vertical layers from the surface to 500 hPa. The grid system of  $M_{CHIMERE}$  is displayed in Figure S4. To run this model,  $0.1^\circ \times 0.1^\circ$  meteorological field is produced by the Weather Research and Forecasting model [Menut et al., 2013]. BC is divided into nine size bins in CHIMERE, and the main features of transport, dry deposition, and wet scavenging of all aerosols are described in Menut et al. [2013]. The global LMDZ-OR-INCA model covers the vertical layer from the surface to 4 hPa, but the regional CHIMERE model only simulates BC up to 500 hPa. As a result, we corrected the BC column load modeled by  $M_{CHIMERE}$  over the North China Plain to account for BC located above 500 hPa. We inferred from the LMDZ-OR-INCA BC distribution that on average over this region, there is 5% BC mass located above 500 hPa. We derived the optimal values of  $\alpha$  by minimizing the deviation between the interpolated BC load and that modeled by CHIMERE over the North China Plain. In detail, considering that the effect of diffusion and transport is different for source and background regions, all model grids were equally divided into three categories according to their BC load (clean  $< 1 \text{ mg m}^{-2}$ , polluted:  $1\text{--}2 \text{ mg m}^{-2}$ , and very polluted  $> 2 \text{ mg m}^{-2}$ ). Note that this is different from our previous study in *R. Wang et al.* [2014a], which applied the same exponent  $\alpha$  for all grid points. Then, different values of  $\alpha$  were tested until achieving the least root-mean-square deviation in each group. These optimized  $\alpha$  were applied for downscaling the modeled BC AAOD over all continents in our best model ( $E_{PKU}/M_{INz}$  over Asia and  $E_{PKU}/M_{IN}$  elsewhere) to  $0.1^\circ \times 0.1^\circ$  in each group of grid points. The derived BC AAOD distribution using this interpolation method is referred to as  $E_{PKU}/M_{DS}$  hereafter and represents our preferred BC distribution.

### 2.6. Estimations of BC Radiative Forcing and Its Uncertainty

We first estimated the all-sky radiative effect of BC at the top of the atmosphere as the difference in short-wave radiative fluxes with and without BC in LMDZ-OR-INCA [Reddy et al., 2005; Hourdin et al., 2006]. The effects in the longwave were neglected as they have been shown to be very small [Reddy et al., 2005]. The RF of BC due to aerosol-radiation interactions was calculated as the change in radiative effect between the preindustrial era (year 1750) using emissions from AeroCom [Dentener et al., 2006] and the present day. The corresponding estimates of the global mean column load, lifetime, mass absorption cross section (MAC), absorption forcing efficiency (AFE), RF, and AAOD of industrial era BC are listed in Table 1, which are compared to the AeroCom Phase I experiments [Schulz et al., 2006]. These estimates were taken as our bottom-up estimates.

According to Bond et al. [2013], the uncertainty in BC RF arises from a combination of uncertainties in BC AAOD and AFE. The uncertainty in BC AAOD itself arises from a combination of uncertainties in the BC emissions, lifetime, and MAC. Therefore, we first computed uncertainties in the BC AAOD averaged over each region by combining uncertainties in the emissions [*R. Wang et al.*, 2014a], lifetime [Bond et al., 2013], and MAC [Bond et al., 2013]. The uncertainty in BC emissions was derived from a Monte Carlo simulation, which accounts for uncertainties in BC emission factors, fuel consumption, and technology fractions. For the lifetime and MAC of BC, we considered the spread of AeroCom models in Bond et al. [2013] as indicative of the uncertainty. After excluding the maximum and minimum values, we derived a 90% uncertainty range of  $\pm 44\%$  for BC lifetime and  $\pm 45\%$  for BC MAC. Finally, we derived the uncertainty in BC RF by combining uncertainties in BC AAOD, "host model" properties [Stier et al., 2013] and the uncertainty in AFE due to vertical profiles [Samset et al., 2013; Hodnebrog et al., 2014]. All these uncertainties are summarized in Table 2.

**Table 2.** Estimation of Uncertainties in the BC RF by the Bottom-Up Method<sup>a</sup>

Uncertainty Source	Basis for the Uncertainty	Calculation of 90% CI
BC emissions (item i)	A Monte Carlo simulation yields a distribution of the estimated emissions in the PKU-BC inventory [R. Wang <i>et al.</i> , 2014a]. The 5% and 95% percentile is 3.1 and 32 Tg yr <sup>-1</sup> , or (-65%, +260%) relative to the central estimate (8.9 Tg yr <sup>-1</sup> ), adopted as the 90% CI. For E <sub>MAC</sub> , according to Bond <i>et al.</i> [2013], the traditional inventory is associated with a relative uncertainty of (-73%, +282%), and this uncertainty is applied for E <sub>MAC</sub> .	The 90% CI relative to the central estimate is derived as (-65%, +260%) for E <sub>PKU</sub> and as (-73%, +282%) for E <sub>MAC</sub> .
BC lifetime (item ii)	BC lifetime varies from 3.3 to 10.6 days [Bond <i>et al.</i> , 2013]. After excluding the maximum and minimum values, the average and standard deviation is 6.2 ± 1.7 days. Hence, a relative standard deviation (RSD) of 27% is adopted.	The 90% CI is derived as ±27% × 1.645 = ±44%
BC MAC (item iii)	BC MAC varies from 4.3 to 15.0 m <sup>2</sup> g <sup>-1</sup> [Bond <i>et al.</i> 2013]. After excluding the maximum and minimum values, the average and standard deviation is 8.5 ± 2.2 m <sup>2</sup> g <sup>-1</sup> . Hence, an RSD of 26% is adopted.	The 90% CI is derived as ±26% × 1.645 = ±43%.
Particle morphology (item iv)	Adachi <i>et al.</i> [2010] found that the bias in the global BC RF would be 6% using a Maxwell Garnett approximation. As the AeroCom study [Bond <i>et al.</i> , 2013] does not cover this factor, we added an uncertainty of ±6% to the MAC.	The 90% CI is ±6%.
Host model uncertainty (item v)	Host model uncertainties for top-of-the-atmosphere all-sky radiative forcing owing to absorption due to differences in radiative transfer models and environmental parameters such as surface albedo and clouds are estimated to lead to an RSD of 11% according to an AeroCom intercomparison study [Stier <i>et al.</i> , 2013].	The 90% CI is derived as ±11% × 1.645 = ±18%
The vertical profiles of BC (item vi)	Samset <i>et al.</i> [2013] isolate the uncertainty of BC RF due to the variability of vertical profiles of BC based on modeled BC vertical profiles from 15 aerosol models. It results in an RSD of 13% around the central estimated BC RF or a 90% CI of ±21%. However, in a more recent study [Hodnebrog <i>et al.</i> , 2014], with a shorter BC lifetime to match the HIPPO observed BC vertical profiles in the model, the global mean forcing efficiency of BC will decrease by 26%. Thus, we adopt a variance of ±26% as a 90% CI for AFE, to account for the impact due to variance in the vertical profiles of BC.	The 90% CI is derived as: ±26%

Overall uncertainty

Based on the uncertainties estimated above, the uncertainty associated with BC RF is calculated by adding all uncertainties (items i–vi) in quadrature by assuming all sources of error are independent. Therefore, for E<sub>PKU</sub>/M<sub>DS</sub>, the 90% confidence intervals should be

$$\text{the lower bound} = -\text{SQRT} ((65\%)^2 + (44\%)^2 + (6\%)^2 + (43\%)^2 + (18\%)^2 + (26\%)^2) = -95\%$$

$$\text{the upper bound} = \text{SQRT} ((260\%)^2 + (44\%)^2 + (6\%)^2 + (43\%)^2 + (18\%)^2 + (26\%)^2) = 270\%$$

It corresponds to a 90% CI of (-95%, +270%) in E<sub>PKU</sub>/M<sub>DS</sub>.

For E<sub>MAC</sub>/M<sub>IN</sub>, the 90% confidence intervals should be the lower bound = -SQRT ((73%)<sup>2</sup> + (44%)<sup>2</sup> + (43%)<sup>2</sup> + (6%)<sup>2</sup> + (18%)<sup>2</sup> + (26%)<sup>2</sup>) = -101%

$$\text{the upper bound} = \text{SQRT} ((282\%)^2 + (44\%)^2 + (43\%)^2 + (6\%)^2 + (18\%)^2 + (26\%)^2) = 290\%$$

It corresponds to a 90% CI of (-101%, +290%) in E<sub>MAC</sub>/M<sub>IN</sub>.

<sup>a</sup>Six uncertainty factors (items i–vi) are considered. All uncertainties are given as 90% confidence intervals (CI).

We note that the AFE of BC (defined as the RF per AAOD at 550 nm) in our model ( $231 \text{ W m}^{-2} \text{ AAOD}^{-1}$ ) is higher than the median value ( $163 \text{ W m}^{-2} \text{ AAOD}^{-1}$ ) of AeroCom Phase I models [Schulz *et al.*, 2006], due to the difference in radiative transfer scheme [Stier *et al.*, 2013] and vertical profiles of BC [Samset *et al.*, 2013]. To achieve an unbiased estimate, the AFE in our model was scaled to the AeroCom median value. Note that the AeroCom models overestimate BC mass at high altitude over the remote oceanic regions [Schwarz *et al.*, 2013], which in turn affects the modeled AFE of AeroCom models. A correction of this bias resulted in a new global AFE of AeroCom models of  $159 \text{ W m}^{-2} \text{ AAOD}^{-1}$  (see supporting information Text S1 and Figure S5), which was adopted here. Samset *et al.* [2014] showed that there is no significant bias in the modeled vertical profile of BC when comparing with the Arctic Research of the Composition of the Troposphere from Aircraft and Satellites campaign over North America or the Aerosol Radiative Forcing in East Asia (A-FORCE) campaign over Japan. Hence, we did not correct the AFE of AeroCom models over these regions.

### 2.7. Estimation of BC Radiation Absorption and Radiative Forcing by a Bayesian Method

To constrain the model, a recent benchmark study by Bond *et al.* [2013] scaled the modeled BC AAOD and thus RF by the ratio of observed to modeled BC AAOD at a relatively small number of locations. However, their scaling method does not properly account for the uncertainties in model and observations. In this study, we replaced the scaling method by Bond *et al.* [2013] with a Bayesian method [Bouttier and Courtier, 1999] to estimate an optimal distribution of BC AAOD and RF. This optimal estimate makes the best account of all model, representativeness, and observational uncertainties. We used the BC AAOD retrieved from AERONET as a constraint over continental regions (section 3.5) and the BC column load measured by the High-performance Instrument Airborne Platform for Environmental Research Pole-to-Pole Observations (HIPPO) campaign as a constraint over three remote oceanic regions (section 3.6). Over the continental regions, we applied the optimal interpolation theory [Lorenc, 1986] to optimize the scaling factor,  $s$ , which was used to scale the BC AAOD from the bottom-up estimate. As we were dealing with scalar quantities in each region, to compute  $s$  and its variance  $V^s$ , the best linear unbiased estimator reduces to

$$s = \frac{V^o}{V^o + V^m} + \frac{V^m}{V^o + V^m} \cdot \frac{o}{m} \quad (3)$$

$$V^s = \frac{V^o \cdot V^m}{V^o + V^m} \cdot \frac{1}{m^2} \quad (4)$$

where  $V^o$  is the error variance of the observations,  $V^m$  is the error variance of the model from the bottom-up method,  $o$  is the average BC AAOD retrieved at the AERONET sites, and  $m$  is the average BC AAOD modeled at the AERONET sites. Next, the error variance of the modeled BC AAOD ( $V^m$ ) was computed from the uncertainties in BC emissions, lifetime, and MAC (as described in section 2.6). The error variance of the observed BC AAOD ( $V^o$ ) was derived as the sum of the error variance of retrieved BC AAOD due to the variance in dust optical properties ( $\pm 18\%$ ) and BC density ( $\pm 5\%$ ) and the error variance due to the representativeness error ( $V^r$ ).  $V^r$ , also called “external representation error” by Engelen *et al.* [2002], represents the uncertainty coming from the scale mismatch when comparing point measurements and their model equivalent. It mostly includes here the spatial variations of the BC AAOD at scales smaller than the model grid boxes and is therefore computed as the mean square of differences in BC AAOD between the (low-resolution) model and a model at the highest resolution that could be achieved in this study. In  $E_{\text{PKU}}/M_{\text{DS}}$ , we assumed  $E_{\text{PKU}}/M_{\text{CHIMERE}}$  to be the “truth,” and  $V^r$  is derived as the mean square of differences in BC AAOD at all AERONET sites modeled by  $E_{\text{PKU}}/M_{\text{DS}}$  and  $E_{\text{PKU}}/M_{\text{CHIMERE}}$  over the North China Plain. We applied this regional  $V^r$  (as a relative uncertainty) over other continental regions as well. In  $E_{\text{MAC}}/M_{\text{IN}}$ , we took  $E_{\text{PKU}}/M_{\text{DS}}$  as the “truth” and computed the mean square of differences in the BC AAOD modeled by  $E_{\text{MAC}}/M_{\text{IN}}$  and  $E_{\text{PKU}}/M_{\text{DS}}$  at all AERONET sites in each region. Then, we added this variance to the  $V^r$  derived above for  $E_{\text{PKU}}/M_{\text{DS}}$  to get the  $V^r$  for the  $E_{\text{MAC}}/M_{\text{IN}}$  model.

The scaling factor  $s$  and its error variance  $V^s$  have the spatial scale of a few measurement sites aggregated together. When applying  $s$  at the scale of continental regions, the error variance  $V^{\text{AAOD}}$  of the resulting BC AAOD was calculated by combining  $V^s$  and a representativeness error for the scaling factor when going from the limited numbers of sites to the whole region ( $V^{\text{diff}}$ ) as

$$V^{\text{AAOD}} = V^s \cdot w^2 + V^{\text{diff}} \quad (5)$$

where  $w$  is the average modeled BC AAOD over each region.  $V^{\text{diff}}$  was calculated as the square of difference between BC AAOD averaged at all AERONET sites and that averaged over the region.  $V^{\text{diff}}$  varies annually, in

particular, for regions with fluctuant natural fires. To account for this interannual variability, we run  $E_{MAC}/M_{IN}$  from 2001 to 2008 to compute the  $V^{diff}$  based on the averaged BC AAOD distributions. In addition, it should be noted that the year 2007 is associated with smaller emissions from biomass burning following the El Niño in 2006. Further simulations for other years would be needed to see this impact on BC amounts and RF. Note that  $V^{diff}$  depends on the location of observation sites and a homogeneous distribution of observation sites covering both low and high BC AAOD regions would reduce  $V^{diff}$ .

For the three remote oceanic regions, we constrained the BC column load (discussed in section 3.6), instead of BC AAOD, in equations (3) and (4). We considered an uncertainty of  $\pm 30\%$  (relative 90% confidence interval) for the observed BC mass concentrations [Schwarz *et al.*, 2013]. The representativeness error variances  $V$  for  $E_{PKU}/M_{DS}$  and  $E_{PKU}/M_{INZ}$  were both calculated as the mean square of the differences of the modeled BC load by  $E_{PKU}/M_{DS}$  and  $E_{PKU}/M_{INZ}$ , as we do not know the *truth*. The variance  $V^{load}$  was computed in a similar way as equation (5) with a representativeness error  $V^{diff}$  computed as the square of the difference between the modeled BC column load averaged at HIPPO sites and that averaged over the whole region.  $V^{AAOD}$  was computed by combining  $V^{load}$  and the variance of BC MAC ( $V^{MAC}$ ).  $V^{MAC}$  was derived as in our bottom-up method.

For the remaining oceanic regions without observations, we applied the modeled BC AAOD from the bottom-up estimate with the associated uncertainty.

As in our bottom-up estimate, uncertainty in BC RF in the Bayesian method was computed by combining uncertainties in the BC AAOD, host model uncertainty and the uncertainty in AFE due to vertical profiles. Finally, the global mean BC RF and the associated uncertainty was estimated by averaging the regional mean BC RF and associated uncertainty weighted by area in each region. The variances ( $V$ ,  $V^o$ ,  $V^m$ ,  $V^s$ ,  $V^{diff}$ ,  $V^{load}$ , and  $V^{AAOD}$ ) in equations 3–5 and those of the BC RF were all expressed in terms of the corresponding values for the lower and upper bounds of the 90% confidences. All variables in the calculation and the procedure to calculate the BC RF and its uncertainty are provided in the supporting information Data Set S1.

### 3. Results and Discussion

#### 3.1. Spatial Distribution of BC Radiation Absorption

We simulated the AAOD due to BC at 900 nm by four inventory/model combinations labeled  $E_{MAC}/M_{IN}$ ,  $E_{PKU}/M_{IN}$ ,  $E_{MAC}/M_{INZ}$ , and  $E_{PKU}/M_{INZ}$ . The main result is that  $E_{PKU}$  gives a different spatial pattern of BC AAOD than  $E_{MAC}$ , particularly over East Asia and central Africa (Figures 1a and 1b). In particular,  $E_{PKU}$ , which was highly disaggregated based on local fuel data [Wang *et al.*, 2013] (e.g., each county in China) and emission factors [e.g., Wang *et al.*, 2012a, 2012b], gives a higher BC AAOD than  $E_{MAC}$  in the north and southwest of China, the northwest of India, and Ganges-Brahmaputra delta. By comparison,  $E_{MAC}$  is developed from generic emission factors, and country-level fuel data disaggregated spatially by assuming a uniform national per capita fuel consumption [Lamarque *et al.*, 2010; Granier *et al.*, 2011]. The subnational data in  $E_{PKU}$  suggest some limitation of the generic  $E_{MAC}$  inventory: for instance, in China, per capita residential coal consumption in northern China ( $4.8 \text{ kg cap}^{-1}$ ) from  $E_{PKU}$  was different from that in southwest China ( $6.0 \text{ kg cap}^{-1}$ ) and in southeast China ( $0.90 \text{ kg cap}^{-1}$ ), whereas  $E_{MAC}$  assumes constant per capita emission for the entire country. Similarly, per capita consumption of fossil fuel in the New Delhi region ( $1.1 \text{ Mg C cap}^{-1}$ ) was 3.3 times in  $E_{PKU}$  larger than the Indian country mean ( $0.33 \text{ Mg C cap}^{-1}$ ). In addition, the larger BC AAOD in western Africa (e.g., in Nigeria) in  $E_{PKU}$  is due to higher BC emission factors applied for the residential sector [R. Wang *et al.*, 2014a], while the decrease in central Africa (e.g., in DR Congo) is a result of less biomass burning in  $E_{PKU}$  using Global Fire Emissions Database (GFED) version 3 fire data [van der Werf *et al.*, 2010] than  $E_{MAC}$  using GFED version 2 fire data [van der Werf *et al.*, 2006]. Meantime, the increased model resolution of  $M_{INZ}$  with  $E_{PKU}$  better captures regional BC AAOD hot spots than  $M_{IN}$  (Figure 1c), illustrating the importance of high-resolution models to take advantage of a high-resolution emission inventory like  $E_{PKU}$ .

#### 3.2. Comparison of Modeled BC AAOD to Observations

The simulated BC AAOD at the 900 nm wavelength was evaluated against AERONET retrievals as monthly means at 213 sites worldwide (see Figure 1b for the distribution of sites) (Figure 2). At most sites,  $E_{PKU}/M_{INZ}$  gives a better agreement with observations in Asia than other simulations. The normalized mean bias

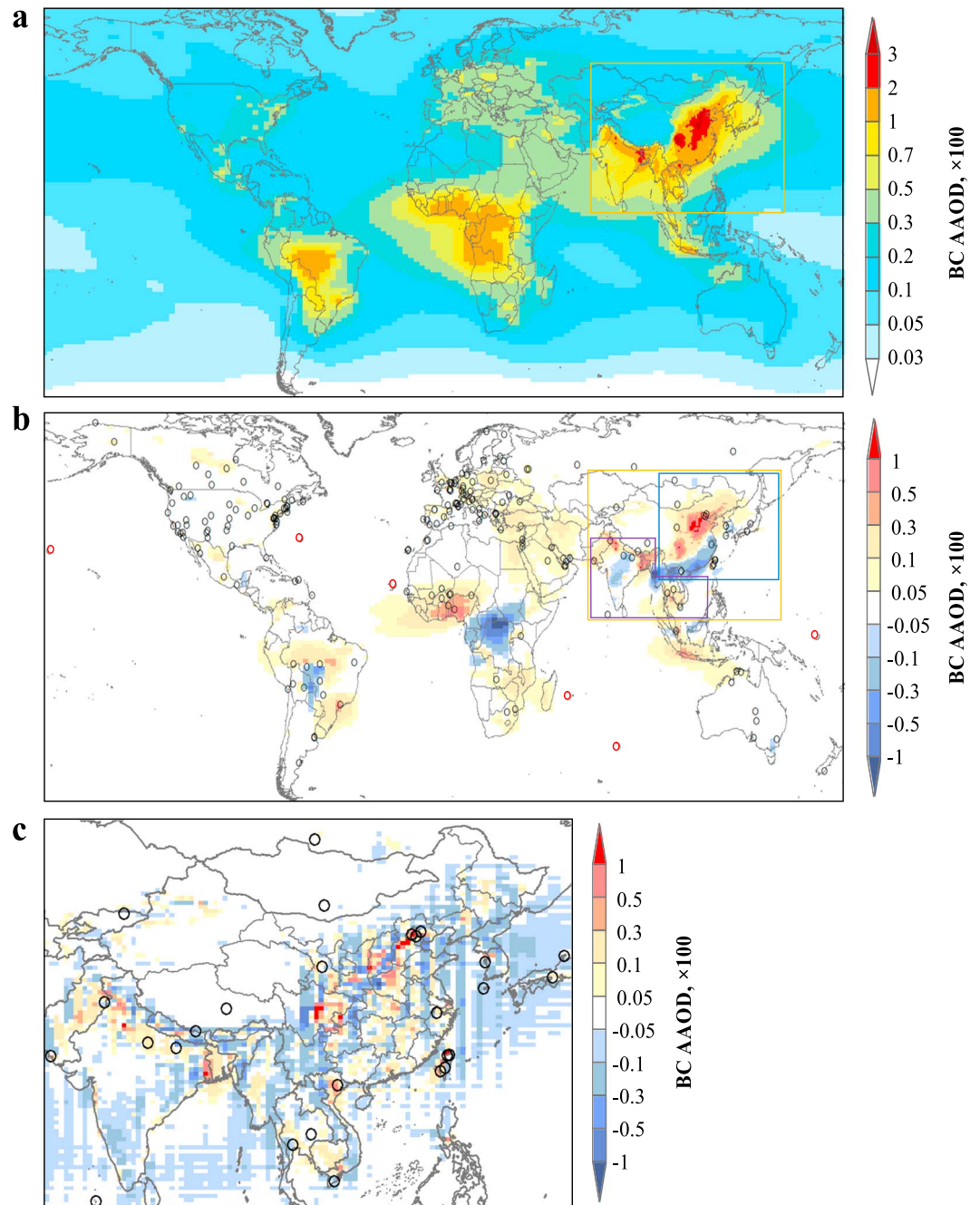


**Figure 1.** Simulated BC AAOD at 900 nm. (a) BC AAOD simulated by  $E_{PKU}/M_{INz}$  over Asia (the orange box) and  $E_{PKU}/M_{IN}$  elsewhere; (b) Simulated BC AAOD as a difference between  $E_{PKU}/M_{INz}$  and  $E_{MAC}/M_{INz}$  over Asia and between  $E_{PKU}/M_{IN}$  and  $E_{MAC}/M_{IN}$  elsewhere. The blue box indicates the region of East Asia, and the purple box the region of South/Southeast Asia. The AERONET sites used to evaluate the model are shown as circles (red circles for oceanic sites). (c) Difference between  $E_{PKU}/M_{INz}$  and  $E_{PKU}/M_{IN}$  over Asia. The simulations are run for 2007, and the observations are taken from AERONET for the same year.

(NMB) quantifies this improvement: the NMB in Asia was reduced from  $-56\%$  in  $E_{MAC}/M_{IN}$  to  $-25\%$  in  $E_{PKU}/M_{INz}$ . Over East Asia, the region with the highest BC emissions, the NMB is reduced from  $-54\%$  to  $-10\%$ , for which the improvement is more significant than that achieved over South/Southeast Asia (NMB reduced from  $-61\%$  to  $-46\%$ ). Comparable improvements are obtained when either the  $E_{PKU}$  inventory or the zoomed model  $M_{INz}$  is used. The former decreases the NMB from  $-41\%$  to  $-25\%$  and the latter from  $-51\%$  to  $-25\%$  in Asia. The improvement of BC AAOD over the non-Asian regions (NMB from  $-71\%$  to

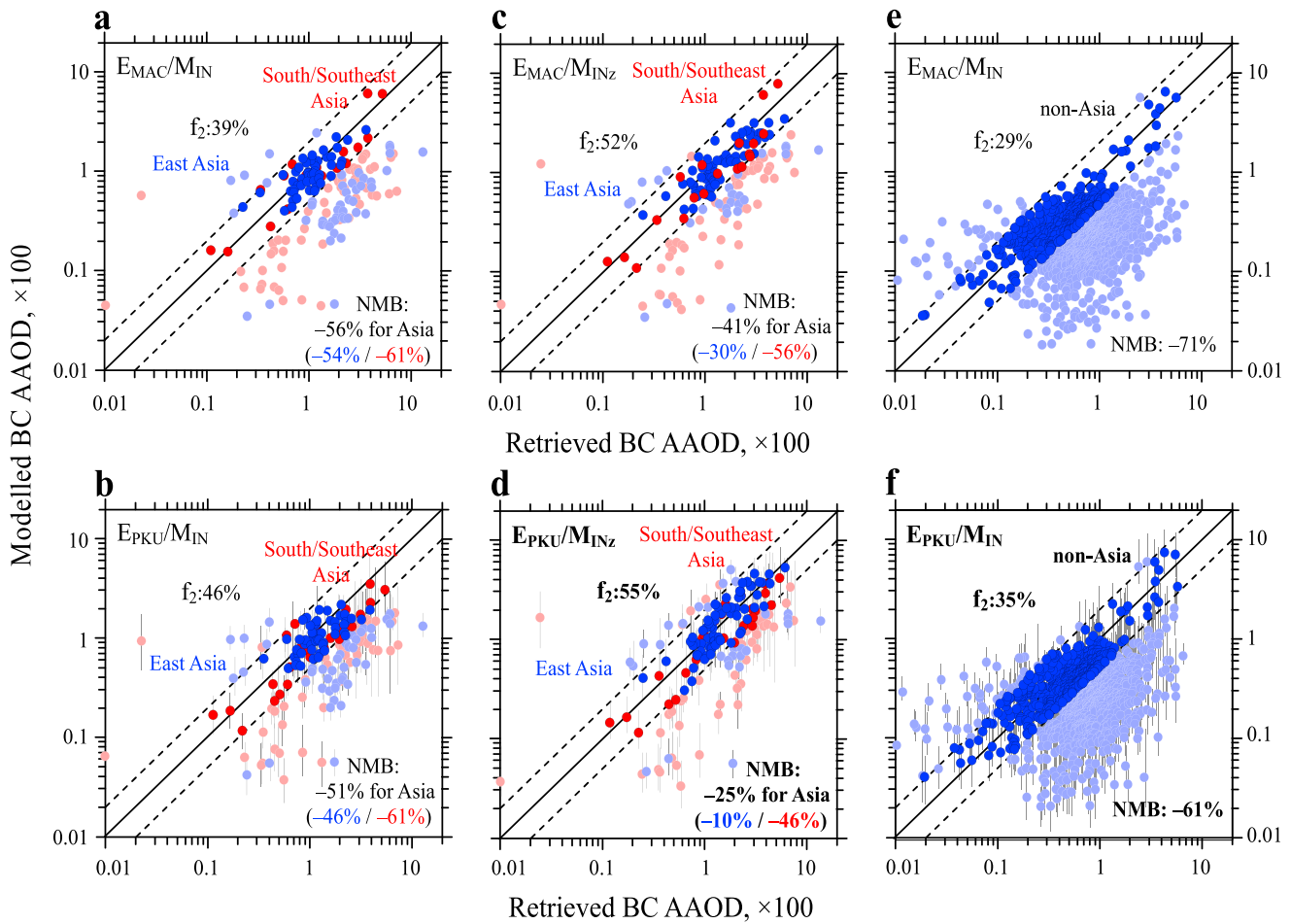


**Figure 2.** (a–d) Comparison of the modeled and retrieved BC AAOD at 900 nm in Asia and (e and f) other regions.  $E_{MAC}/M_{IN}$  (Figures 2a and 2e);  $E_{PKU}/M_{IN}$  (Figures 2b and 2f);  $E_{MAC}/M_{INZ}$  (Figure 2c);  $E_{PKU}/M_{INZ}$  (Figure 2d). Modeled BC AAOD are averaged over the same days as observations in each month. The vertical bars in Figures 2b and 2d represent the values obtained with the first and third quartiles of the  $E_{PKU}$  inventory. Normalized mean bias (NMB) and the percentage of sites with modeled BC AAOD within a factor of 2 of the observations ( $f_2$ ) are also shown. NMB for East Asia (blue) and South/Southeast Asia (red) are indicated in Figures 2a–2d.

–61%) is not as significant as it is over Asia, mainly due to a relatively coarser model resolution over these regions. We also compared the modeled BC column load with that retrieved from the AERONET observations in Figure S6. There is a comparable improvement as we observed for BC AAOD, with the NMB being reduced from –60% for  $E_{MAC}/M_{IN}$  to –35% for  $E_{PKU}/M_{INZ}$  over Asia. The remaining bias suggests that improving the emission inventory and enhancing the model resolution do not suffice to remove all bias in the model.

### 3.3. Downscaling of BC AAOD to 10 km Resolution

Even though  $E_{PKU}/M_{INZ}$  provides a better agreement with observations in Asia, such a fine spatial resolution cannot be applied globally due to heavy computational cost. In particular, for the rest of the world outside the zoom over Asia, BC AAOD remains underestimated by 61% in  $E_{PKU}/M_{IN}$  (Figure 2). We investigated the effect of a downscaling method as used in *R. Wang et al.* [2014a] on the simulated BC AAOD.

Figure 3 shows the variation of the root-mean-square deviation (RMSD) in the comparison of BC column load modeled by CHIMERE and that interpolated by equation (2) under different values of the exponent  $\alpha$ . It is found that the lowest RMSD can be achieved for polluted and very polluted grids by using  $\alpha$  values of 0.03 and 0.09, respectively, while RMSD is weakly dependent on  $\alpha$  for clean grids ( $\alpha = 0$ ). This is reasonable because the spatial distribution of BC over the clean areas is mainly controlled by long-range transport of pollutants from remote grids, rather than local emissions, and thus, the exponent  $\alpha$  is close to zero. These  $\alpha$  are smaller than the value (0.30) calibrated for surface BC concentrations [*R. Wang et al.*, 2014b], confirming that column

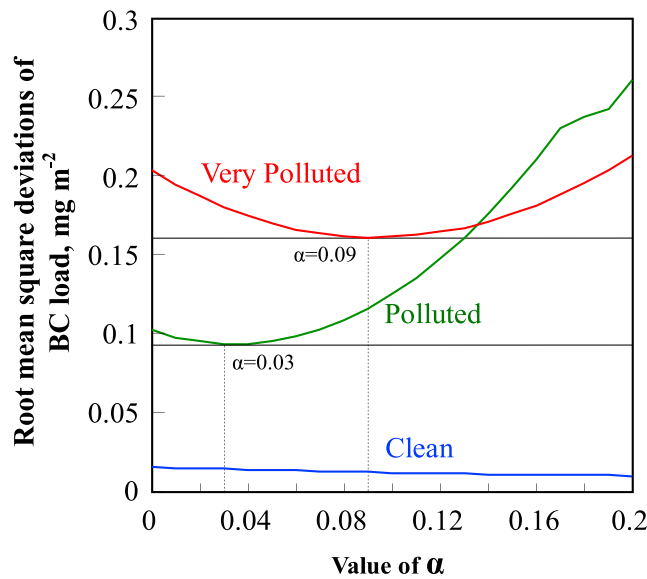


**Figure 3.** Variation of the root-mean-square deviation in the comparison of BC load for all 10 km grids in the North China Plain downscaled from  $E_{PKU}/M_{INz}$  and modeled by  $E_{PKU}/CHIMERE$  under different values of  $\alpha$ . Considering that the effects of diffusion are different for polluted and clean areas, all grids are categorized equally into three groups according to the modeled BC load (clean  $< 1 \text{ mg m}^{-2}$ , polluted:  $1\text{--}2 \text{ mg m}^{-2}$ , and very polluted  $> 2 \text{ mg m}^{-2}$ ).

is no guarantee that this method can be extended as such to all regions. We run sensitivity experiments to test the impact of using larger or smaller  $\alpha$  when estimating the RF of BC in section 3.7. It is important meanwhile to put emphasis on the development of global high-resolution aerosol models.

It is known that the total AOD retrieved from AERONET is more uncertain under low aerosol optical depth (AOD) [Dubovik and King, 2000], because the retrievals of single scattering albedo ( $\omega_0$ ) are more uncertain at low AOD and thus removed from Version 2.0 data product. In our study, the missing  $\omega_0$  in Version 2.0 data was recovered from Version 1.5 data product. A similar approach was taken by Bond et al. [2013]. They showed that the retrieved AOD in this way is very similar to that derived by applying the  $\omega_0$  retrieved from high AOD observations to all AOD values at each station. Therefore, we do not account for the additional

load is less dependent on emissions than surface concentrations. Figure S7 shows that the correlation coefficient between the concentrations modeled by CHIMERE and the BC surface emissions decrease with altitude.

Using these “calibrated” exponents, we were able to downscale the modeled BC AAOD in Figure 1a to 10 km resolution ( $E_{PKU}/M_{DS}$ ) to get closer to the resolution of point AERONET measurements. There are two points that support use of this method. First,  $E_{PKU}/M_{DS}$  can faithfully reproduced the CHIMERE modeled gradients of BC column load over the North China Plain (Figure 4). Second, with the downscaling method, the bias (NMB) of modeled BC AAOD to observations gets further reduced from  $-25\%$  to  $-5\%$  over Asia, from  $-60\%$  to  $-45\%$  over the other regions, lending certain confidence to its use over other regions (Figure 5). Nevertheless, there

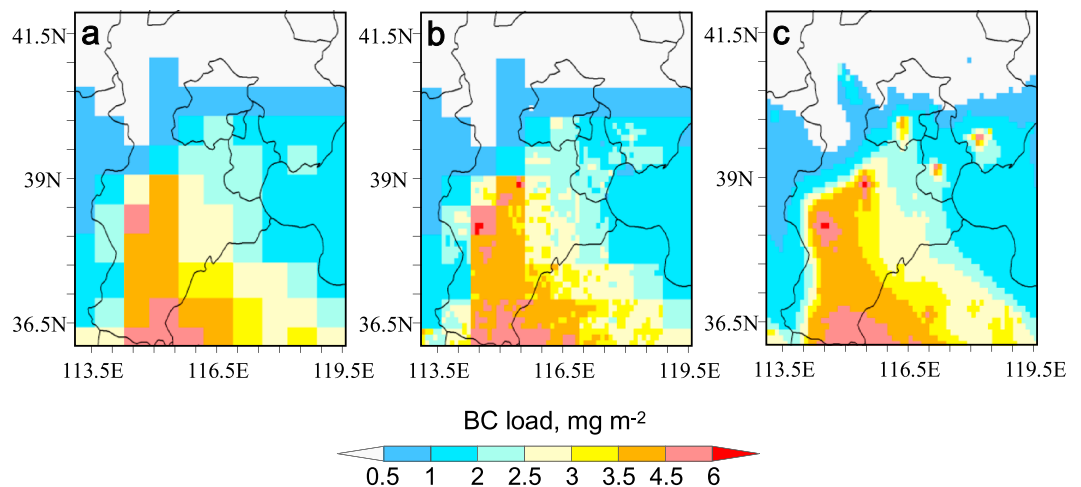


**Figure 4.** Spatial distributions of the BC column load ( $\text{mg m}^{-2}$ ) by different models. (a) BC column load modeled by  $E_{PKU}/M_{INz}$ . (b) BC column load modeled by using the downscaling method ( $E_{PKU}/M_{DS}$ ). (c) BC column load directly modeled by  $E_{PKU}/CHIMERE$ .

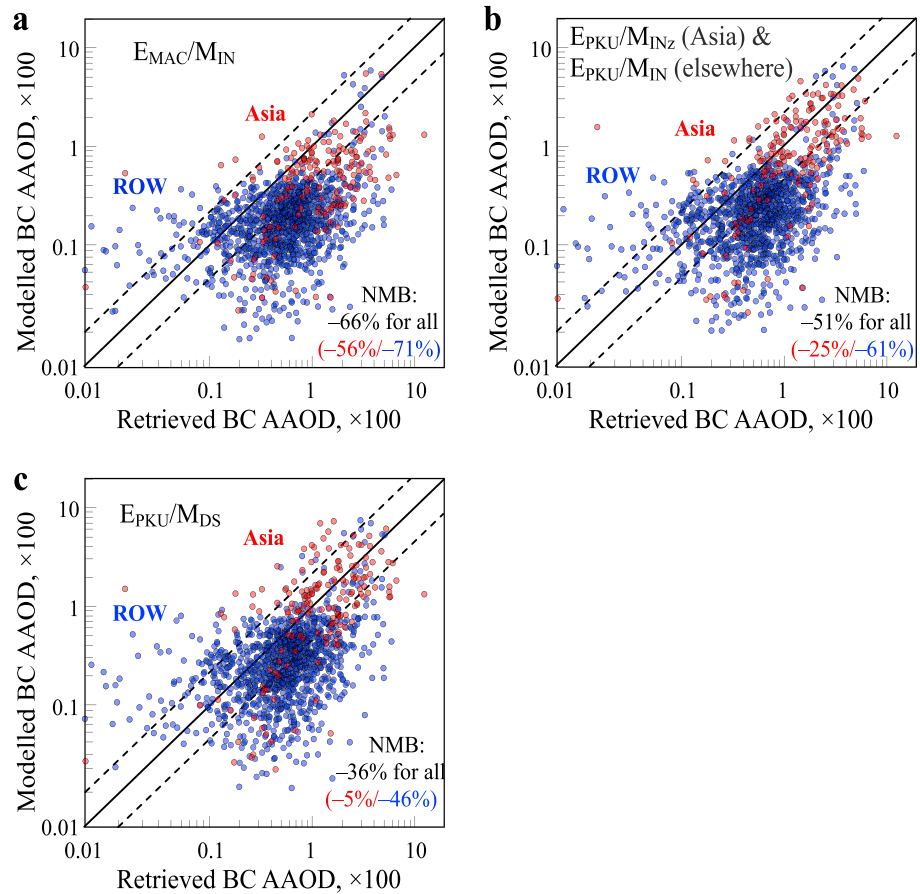


**Figure 5.** Comparison of the modeled and retrieved BC AAOD at 900 nm (monthly mean) in Asia (red) and the rest of the world (ROW) region (blue) by different models. (a)  $E_{MAC}/M_{IN}$ . (b)  $E_{PKU}/M_{INz}$  in Asia and  $E_{PKU}/M_{IN}$  elsewhere. (c) Downscaled to a resolution of 10 km from  $E_{PKU}/M_{INz}$  (over Asia) and from  $E_{PKU}/M_{IN}$  (over ROW) using an emission-based power law function (namely, as  $E_{PKU}/M_{DS}$ ). Modeled and retrieved BC AAOD are averaged for the same days as AERONET observations in each month. Normalized mean bias (NMB) for all points is shown in each panel, with the numbers for Asia (red) and ROW (blue) indicated in parentheses.

uncertainty due to use of retrieved AAOD at low AOD in our study. We verified that the deviation between modeled and observed monthly mean BC AAOD increased with decreasing AOD (Figure S8). We did not exclude the data with the AOD less than 0.4, because these data represent the region with low aerosol loads. Note that the fraction of AERONET sites out of Asia with the observed monthly AOD (430 nm) less than 0.3 (or 0.4) is 76% (85%), higher than the fraction of 30% (44%) in Asia. More in situ measurements which can be compared with AERONET measurements [e.g., Corrigan et al., 2008; Esteve et al., 2012] are necessary to assess the impact.

**3.4. Location Bias of the AERONET Sites With Respect to BC**

The AERONET network [Holben et al., 1998; Dubovik and King, 2000] provides the best data set of aerosol absorption in the shortwave at over 500 sites worldwide. Sato et al. [2003] used it to calibrate their global aerosol climatologies produced by transport models and found that BC concentrations need to be increased by a factor of 2 to 4 to agree with observations, leading to a climate forcing by BC of  $\sim 1 \text{ W m}^{-2}$ . Other studies further refined the method and come to similar conclusions, i.e., an upward revision of BC RF [Chung et al., 2005, 2012; Ramanathan and Carmichael, 2008; Bond et al., 2013]. However, the reason for the underestimation of radiation absorption by aerosols is not well understood. One novelty of our work is to reduce the discrepancy by increasing model resolution and using a highly spatially disaggregated emission inventory. To understand the reason for the underestimation of BC in coarse-resolution models, Figure 6a presents the histogram of AERONET sites on basis of BC AAOD within  $2^\circ \times 2^\circ$  grids as a typical resolution used in previous

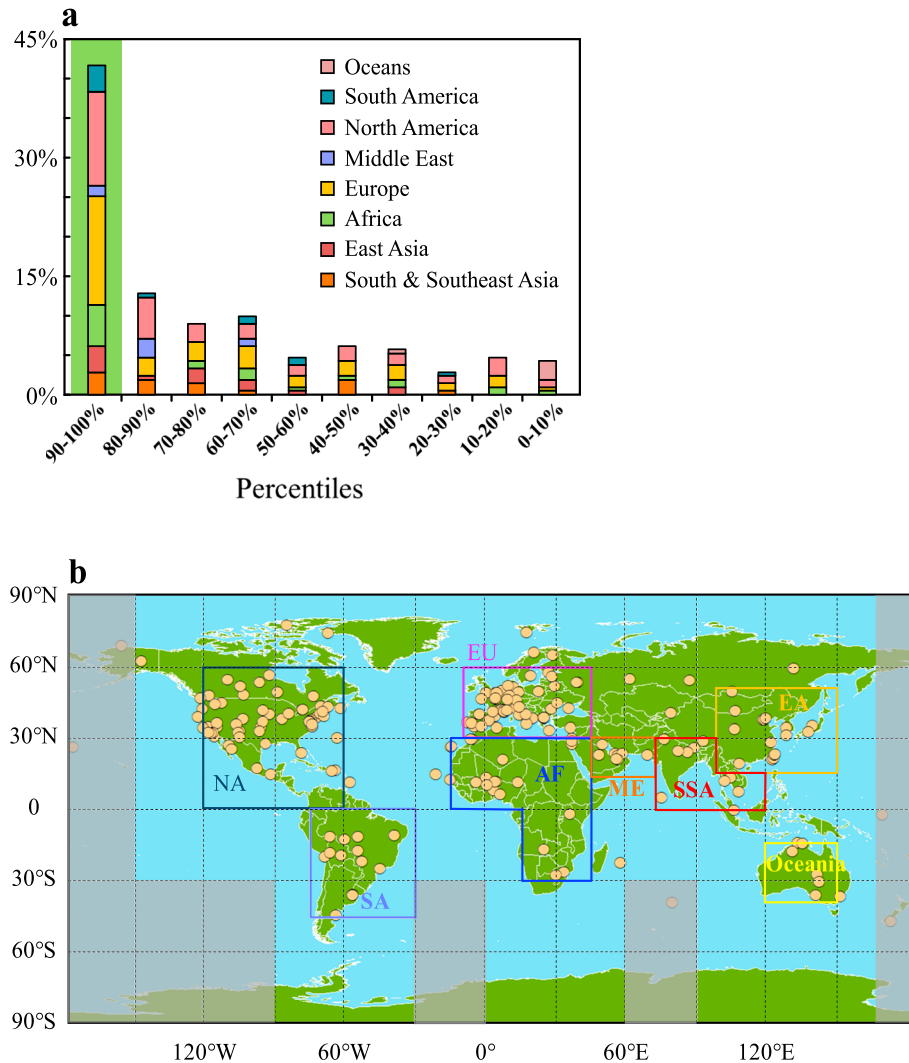


**Figure 6.** (a) Histogram of the AERONET sites on basis of BC AAOD within a coarse grid of  $2^\circ \times 2^\circ$ . For a coarse model grid of  $2^\circ \times 2^\circ$ , there are 400 subgrids of  $0.1^\circ \times 0.1^\circ$ . We derive the BC AAOD from  $E_{PKU}/M_{DS}$  for all  $0.1^\circ \times 0.1^\circ$  subgrids and then compute the percentile of BC AAOD the AERONET site locates among all  $0.1^\circ \times 0.1^\circ$  subgrids. (b) Distribution of all AERONET sites. Globe was divided into eight major source regions (North America (NA), South America (SA), Europe (EU), Africa (AF), Middle East (ME), South/Southeast Asia (SSA), East Asia (EA), and Oceania), three remote oceanic regions (grey shaded area), and the remaining oceanic regions.

models. The figure illustrates that a large fraction (41%) of AERONET sites are located in the top 90th percentile of BC AAOD in a coarse model grid of  $2^\circ \times 2^\circ$ . In other words, the AERONET sites are biased to polluted locations in these grids. This makes the underestimation of BC AAOD found in previous studies sensitive to the spatial distribution of BC within a coarse model grid. In fact, the location of the AERONET site stems from two constraints: a site has to be accessible which favors populated regions, and a strong signal is needed to invert the radiances [Holben *et al.*, 1998]. This sampling bias toward polluted locations transfers to a representativeness error when comparing observations with coarse-resolution models and estimating the observation-constrained RF of BC.

**3.5. Regional BC AAOD and Direct Radiative Forcing**

We followed three approaches to estimate the regional mean BC AAOD and RF with their associated uncertainties. First, we derived the BC AAOD and RF from the LMDZ-OR-INCA model as our bottom-up estimates (see methods in section 2.6). Second, we followed the approach by Bond *et al.* [2013] to scale the modeled BC AAOD to match the simulated BC AAOD with observations, derived as a scaling estimate. At last, a

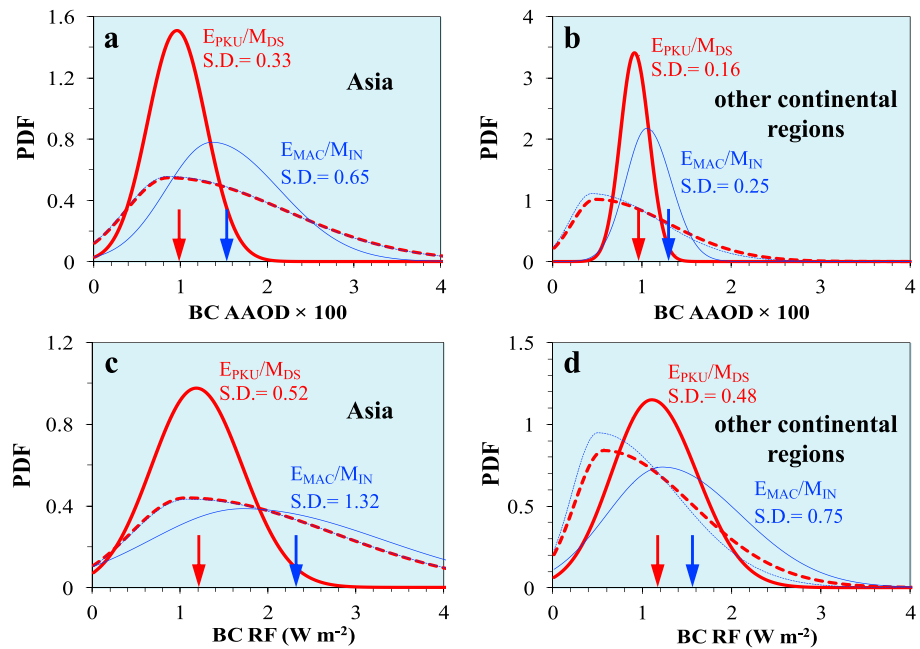


**Figure 7.** Uncertainty ranges of (a and b) BC AAOD at 550 nm and (c and d) BC RF over Asia and other continental regions. The probability density functions (PDF) of Bayesian estimates from  $E_{PKU}/M_{DS}$  (red lines) and  $E_{MAC}/M_{IN}$  (blue lines) are shown as solid lines, and the PDFs of bottom-up estimates are shown as dashed lines. The estimates based on the scaling method are shown as arrows without a distribution. The standard deviations (SD) for Bayesian estimates are listed in each panel.

Bayesian method was applied to constrain the model by observations, derived as our Bayesian estimates (see methods in section 2.7). Figure 7 shows the uncertainty distributions of optimal and a priori BC AAOD and RF as an average over Asia and other continental regions. As a result, the optimal estimate delivers an intermediate value between the bottom-up and scaling estimates, but the associated large uncertainty in the bottom-up estimate gets reduced by using observations as a constraint. Note that the high-resolution model and new inventory improves the spatial distribution of BC and thus reduces the representativeness error associated with coarse-resolution model and spatially biased emission inventory. Replacing  $E_{MAC}/M_{IN}$  with  $E_{PKU}/M_{DS}$  reduces the uncertainty (standard deviation) in the Bayesian estimate by 49% (from 0.65 to 0.33) and 36% (from 0.25 to 0.16) for BC AAOD, and by 61% (from 1.32 to 0.52) and 36% (from 0.75 to 0.48) for BC RF over Asia and other continental regions, respectively (Figure 7).

### 3.6. Column Load of BC Over the Oceanic Regions

Up to now, we have constrained the BC AAOD and thus RF over continents. However, the modeling of BC RF over the oceans is associated with higher uncertainty, indicated by surface BC concentrations in the Arctic [Shindell *et al.*, 2008] and vertical profiles of BC over the oceans [Schwarz *et al.*, 2013]. We compared the modeled BC volume mixing ratios to in situ observations measured over the remote central Pacific Ocean from 85° N to 67°S during the High-performance Instrument Airborne Platform for Environmental Research Pole-to-Pole Observations research aircraft campaign (HIPPO) [Wofsy *et al.*, 2011; Wofsy, 2012] (Figure 8). The simulated BC volume mixing ratios were overestimated by an average factor of 5 above 6 km when compared to HIPPO, as are most AeroCom models [Schwarz *et al.*, 2013]. Most current models, although not all of them, overestimate the BC concentrations measured by HIPPO at high altitudes [Schwarz *et al.*, 2013]. Although some recent studies showed that a shorter BC lifetime can reduce this bias, there is still overestimation of BC, in particular, over the latitude band of 60°N–90°N [Q. Q. Wang *et al.*, 2014; X. Wang *et al.*, 2014]. Samset *et al.* [2014] showed that a shorter BC lifetime is helpful, but it is not sufficient to reduce all biases. More studies addressing the impact of meteorology and microphysics of BC, such as the work by Kipling *et al.* [2013], Q. Q. Wang *et al.* [2014], X. Wang *et al.* [2014], and Zhang *et al.* [2015] are needed to improve the models. In our study, we defined three remote oceanic regions in Figure 6b, which can be represented by the regions covered by HIPPO measurements. We constrained the modeled BC column load and thus BC AAOD over the

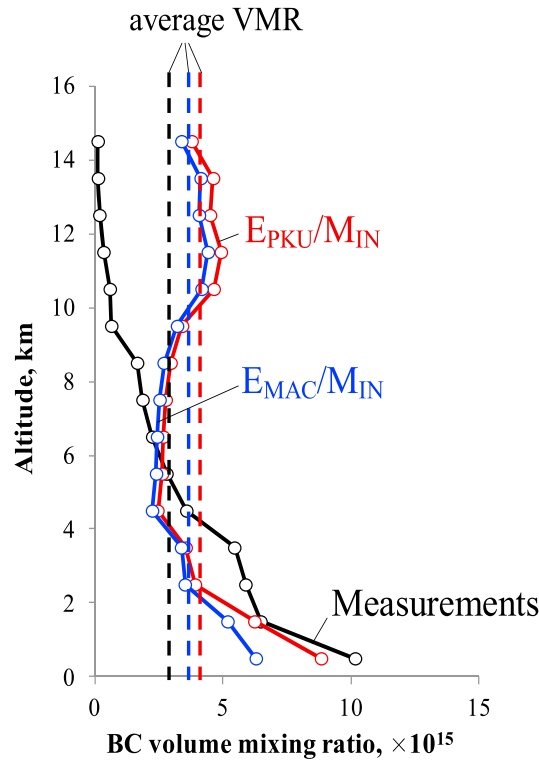


**Figure 8.** Comparison of the BC volume mixing ratios over the remote Pacific Ocean region modeled by  $E_{PKU}/M_{IN}$  and  $E_{MAC}/M_{IN}$  and that measured by the High-performance Instrumented Airborne Platform for Environmental Research Pole-to-Pole Observations (HIPPO) research aircraft campaign [Wofsy *et al.*, 2011, 2012]. The model is run for 2007, and the measurement is taken as an average for the period from 2009 to 2011. The interannual variations are not considered in our comparison. Measured monthly averaged BC volume mixing ratios (local pressure and temperature) for each 1 km height layer are shown with a solid black line, and simulated monthly averaged BC volume mixing ratios collocated with measurements are shown, respectively, in blue ( $E_{MAC}/M_{IN}$ ) and red ( $E_{PKU}/M_{IN}$ ) solid lines. The volume mixing ratios over each vertical layer are averaged and shown as dashed lines.

remote oceanic regions using the BC column load derived from the HIPPO measurements (see methods in section 2.6). The BC column load from HIPPO was derived by integrating the vertical profile of the measured mean BC volume mixing ratio at different locations (Figure 8). We used HIPPO measurements, rather than continental AERONET sites, to constrain our model, because of the scarcity of AERONET sites over the oceans. It should be noted that the remote oceanic regions cover only 30% in the total area of the oceans. There are no observations that can be used to constrain the modeled BC AAOD over the remaining oceanic regions, and we applied the modeled BC AAOD and RF with the associated high uncertainty.

### 3.7. Global Direct Radiative Forcing of BC

The global mean BC RF was calculated for both  $E_{MAC}/M_{IN}$  and  $E_{PKU}/M_{DS}$  by three approaches: a bottom-up method ( $F_M$ ), a scaling method ( $F_S$ ), and a Bayesian method ( $F_B$ ). The three estimates are compared in Figure 9. In  $E_{MAC}/M_{IN}$ , the global mean BC RF estimated by the bottom-up ( $0.35 \text{ W m}^{-2}$ ) and scaling ( $0.65 \text{ W m}^{-2}$ ) method differ by 85%, as are previous studies [Sato *et al.*, 2003; Chung *et al.*, 2005, 2012; Ramanathan and Carmichael, 2008; Bond *et al.*, 2013]. In contrast, in  $E_{PKU}/M_{DS}$ , as our best attempt to simulate the BC absorption at

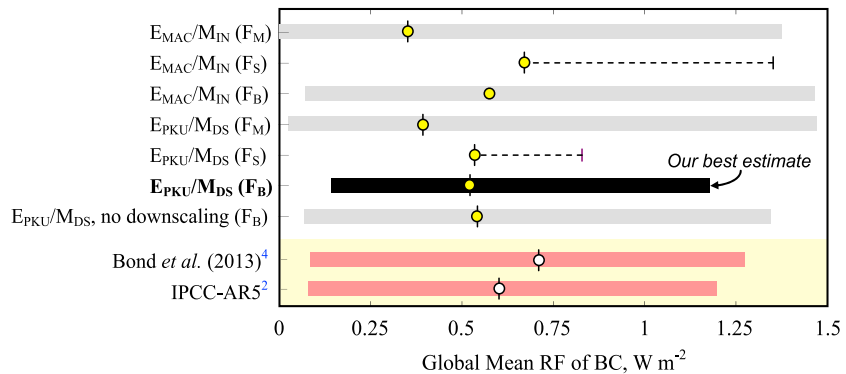


**Figure 9.** Comparison of the bottom-up ( $F_M$ ), scaling ( $F_S$ ), and Bayesian ( $F_B$ ) estimates of global mean BC RF. The central estimates are shown as circles, while 90% uncertainty ranges are shown as error bars. Our estimated global mean BC RF is compared with that in the literature [Bond *et al.*, 2013] and the Fifth Assessment Report of the Intergovernmental Panel on Climate Change (IPCC-AR5) [Boucher *et al.*, 2013]. The dashed lines in  $F_S$  show the results by scaling BC RF over all oceans using AERONET observations, as done in the literature.  $F_B$  without downscaling (using results by  $E_{PKU}/M_{IN}$  over Asia and  $E_{PKU}/M_{IN}$  elsewhere) is also shown.

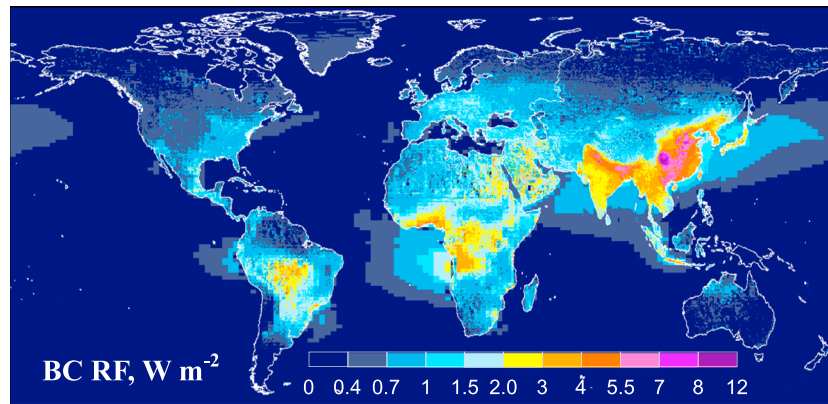


**Figure 10.** Global map of annual mean RF of BC derived at a high resolution of  $0.1^\circ \times 0.1^\circ$ . The gridded BC RF is calculated based on the simulated BC AAOD at  $0.1^\circ \times 0.1^\circ$  resolution from the combination of  $E_{PKU}/M_{DS}$ , and then the BC RF averaged over each continent and oceanic regions are normalized to that in our Bayesian estimates.

high resolution, the difference between the global mean  $F_M$  ( $0.39 \text{ W m}^{-2}$ ) and  $F_S$  ( $0.54 \text{ W m}^{-2}$ ) gets reduced to 38%, reflecting a better agreement of the modeled BC AAOD with observations. Finally, as an “assimilation compromise,” the global mean RF of BC estimated by the Bayesian method delivers an intermediate value between  $F_M$  and  $F_S$ . The global mean  $F_B$  estimated by  $E_{MAC}/M_{IN}$  ( $0.58 \text{ W m}^{-2}$ ) and  $E_{PKU}/M_{DS}$  ( $0.53 \text{ W m}^{-2}$ ) is close to each other, while  $F_S$  is higher in  $E_{MAC}/M_{IN}$  ( $0.68 \text{ W m}^{-2}$ ) than that in  $E_{PKU}/M_{DS}$  ( $0.54 \text{ W m}^{-2}$ ). In either  $E_{PKU}/M_{DS}$  or  $E_{MAC}/M_{IN}$ , the  $F_B$  ( $0.53$  or  $0.58 \text{ W m}^{-2}$ ) is higher than the  $F_M$  ( $0.39$  or  $0.35 \text{ W m}^{-2}$ ), because the modeled BC AAOD is lower than that retrieved from AERONET. In  $E_{PKU}/M_{DS}$ , due to application of the Bayesian approach, the 90% uncertainty range of BC RF was reduced from  $-95\%/+270\%$  in  $F_M$  to  $-72\%/+125\%$  in  $F_B$ . As revealed in our study, there is a significant representativeness error in  $E_{MAC}/M_{IN}$  due to the use of the spatially biased emission inventory and coarse model resolution. As a result, the Bayesian estimate gives less weight to observations when constraining the model. Despite similar central estimates, the 90% uncertainty range associated with the global mean  $F_B$  is reduced from  $-88\%/+155\%$  in  $E_{MAC}/M_{IN}$  to  $-72\%/+125\%$  in  $E_{PKU}/M_{DS}$ , mainly due to a reduced representativeness error.

Downscaling the simulated BC AAOD to 10 km resolution reduces the misfit of modeled to observed BC AAOD (Figure 5) and thus the representativeness error. In a sensitivity test without downscaling (only using  $E_{PKU}/M_{INz}$  over Asia and  $E_{PKU}/M_{IN}$  elsewhere), the global mean  $F_B$  would be  $0.54 \text{ W m}^{-2}$ , but with a 90% uncertainty range of  $0.07\text{--}1.34 \text{ W m}^{-2}$  (Figure 9). Although the central estimate was not influenced too much, the uncertainty is 22% larger than that in  $E_{PKU}/M_{DS}$ . Note that the power law exponents used in the downscaling method are calibrated using the data simulated by CHIMERE over one specific region. Sensitivity tests show that a one third increase or decrease of the exponents change the global mean  $F_B$  from 0.50 to  $0.58 \text{ W m}^{-2}$ . Hopefully,  $0.1^\circ \times 0.1^\circ$  resolution modeling of BC, as done here with CHIMERE over North China Plain, can be performed globally in the future to reduce this uncertainty.

### 3.8. Spatial Distribution of BC Radiative Forcing

In spite of a lower estimate of the global BC RF, the produced  $0.1^\circ \times 0.1^\circ$  map of BC RF reveals high perturbation of BC to local radiation balance, given the large values of the RF induced by BC over polluted regions, typically larger than  $7.0 \text{ W m}^{-2}$  (Figure 10). *Srekanth et al.* [2007] used a seven-channel aethalometer to measure the BC mass concentrations and estimate the shortwave RF of BC using the Santa Barbara DISORT Atmospheric Radiative Transfer model. They estimated a BC radiative effect of  $3.9 \text{ W m}^{-2}$ , in agreement with a BC RF of  $4.0 \text{ W m}^{-2}$  from our Bayesian estimate over the region. The high RF values, more than twice the total RF from all well-mixed greenhouse gases ( $2.83 \text{ W m}^{-2}$ ) [*Myhre et al.*, 2013b], and the associated atmospheric heating may have a significant impact on the water cycle and atmospheric circulation at local and regional scales.

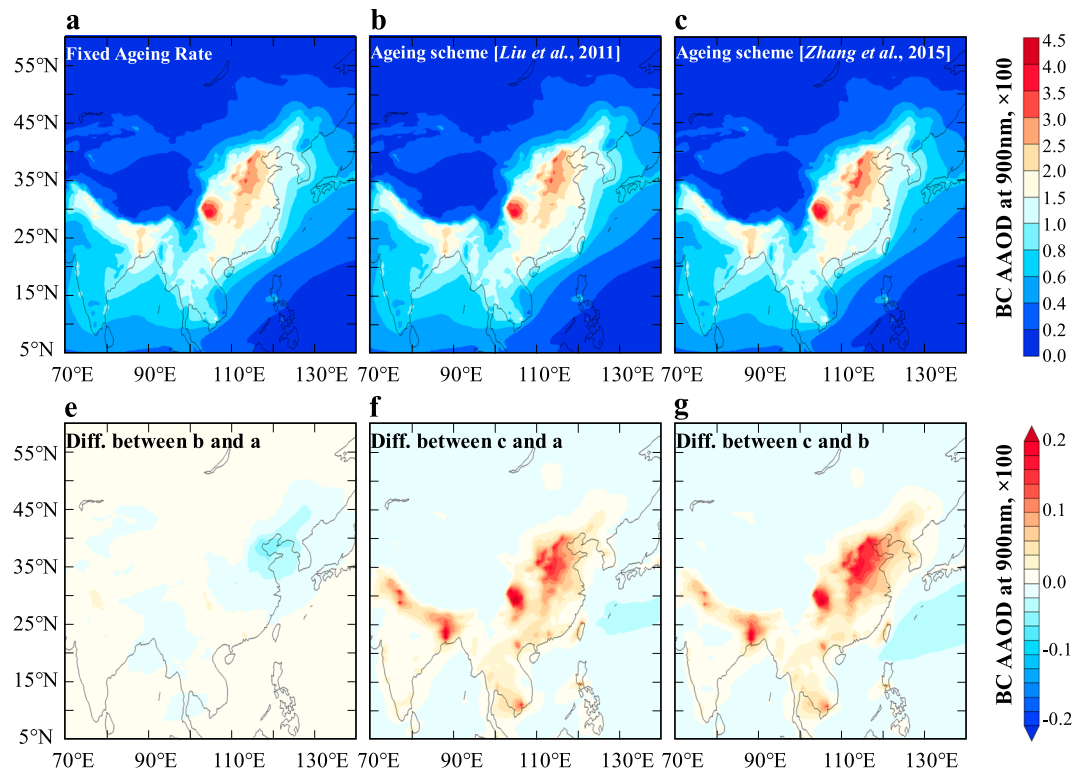


**Figure 11.** (a–c) Comparison of BC AAOD over Asia modeled by  $E_{PKU}/M_{INZ}$  using three BC aging schemes: (a) the prescribed constant time scale of aging; (b) BC aging scheme by Liu et al. [2011]; (c) BC aging scheme by Zhang et al. [2015]. (d–f) Difference of modeled BC AAOD between Figures 11b and 11a (Figure 11d), Figures 11c and 11a (Figure 11e), and Figures 11c and 11b (Figure 11f).

#### 4. Sensitivity of BC RF to the Aging Scheme

Condensation, coagulation, and photochemical oxidation change the mixing state of BC with other aerosol species [Jacobson, 2001; Riemer et al., 2010; Oshima et al., 2009]. It affects the BC lifetime by controlling the fraction of soluble BC that can be removed by wet scavenging [Cooke and Wilson, 1996; Stier et al., 2005] as well as the optical properties of BC [Jacobson, 2001; Bond et al., 2006; Oshima et al., 2009]. The sectional method [Jacobson, 2001; Adams and Seinfeld, 2002; Spracklen et al., 2005; Oshima et al., 2009; Riemer et al., 2009] is the most realistic approach for modeling the mixing state of BC but requires too many tracers, making it hard to be implemented in a general circulation model (GCM) such as LMDZ-OR-INCA. Modal methods were adopted in some GCMs to account for aerosols mixing based on condensation and coagulation, such as European Centre/Hamburg (ECHAM5-HAM) [Stier et al., 2005], MADE-in [Aquila et al., 2011], GISS-MATRIX [Bauer et al., 2010; Bauer and Menon, 2012], CAM-MAM7 [Liu et al., 2012] and Weather Research and Forecasting (WRF)-chem-MOSAIC [Matsui et al., 2013]. It is demonstrated that simulating the aging of BC from fresh mode to internally mixed accumulation mode based on condensation and coagulation is important near fossil fuel sources [Ghan et al., 2012]. However, as pointed out by Oshima and Koike [2013], more than half of 15 models included in the AeroCom Phase II experiment [Myhre et al., 2013a] used a constant time scale for the BC aging (including LMDZ-OR-INCA) or ignore the aging processes. For these reasons, we tested the impact by implementing the BC aging schemes by Liu et al. [2011] and Zhang et al. [2015] in our model.

The BC aging rate depends on condensation of sulphate, chemical oxidation, and coagulation between different particles. In general, the aging rate is dominated by condensation. Hence, Koch [2001] and Wilson et al. [2001] modeled the aging rate based on the production of gas-phase sulfuric acid. Liu et al. [2011] further improved this method in Geophysical Fluid Dynamics Laboratory’s chemistry and climate model (AM3). Accordingly, the aging rate of BC can be represented as

$$k = \beta[\text{OH}] + \alpha \tag{6}$$

where [OH] is the atmospheric hydroxyl (OH) radical concentrations from LMDZ-OR-INCA,  $\beta$  represents a fast aging process by condensation, and  $\alpha$  represents a slow aging process by coagulation. According to Liu et al.

**Table 3.** Sensitivity of the BC RF to Different Aging Schemes of BC in  $E_{PKU}/M_{DS}^a$

	Fixed Aging Rate				Aging [Liu et al., 2011]				Aging [Zhang et al., 2015]			
	$F_M(W m^{-2})$	$o/m$	$s$	$F_B(W m^{-2})$	$F_M(W m^{-2})$	$o/m$	$s$	$F_B(W m^{-2})$	$F_M(W m^{-2})$	$o/m$	$s$	$F_B(W m^{-2})$
EA	1.170	0.972	0.973	1.139	1.142	0.984	0.985	1.125	1.236	0.926	0.928	1.147
SSA	0.911	1.578	1.555	1.416	0.905	1.567	1.545	1.398	0.967	1.459	1.441	1.394
Africa	0.825	2.660	2.516	2.077	0.826	2.663	2.519	2.080	0.849	2.606	2.466	2.093
Europe	0.561	1.848	1.786	1.003	0.550	1.858	1.796	0.987	0.574	1.826	1.766	1.014
ME	1.087	1.536	1.512	1.643	1.099	1.524	1.501	1.649	1.098	1.560	1.535	1.686
NA	0.366	2.482	2.354	0.862	0.386	2.461	2.335	0.900	0.369	2.464	2.337	0.862
SA	0.543	1.170	1.166	0.633	0.528	1.198	1.194	0.630	0.554	1.149	1.146	0.634
OCE	0.237	1.759	1.655	0.392	0.240	1.708	1.612	0.387	0.232	1.779	1.673	0.389
Ocean(HIPPO)	0.194	0.679	0.690	0.134	0.220	0.639	0.652	0.144	0.189	0.718	0.728	0.138
Ocean(other)	0.307			0.307	0.336			0.336	0.306			0.306
Land	0.670			1.181	0.668			1.186	0.691			1.186
<b>Global</b>	<b>0.394</b>			<b>0.527</b>	<b>0.414</b>			<b>0.545</b>	<b>0.400</b>			<b>0.529</b>

<sup>a</sup>This table compares a constant BC aging rate prescribed in LMDZ-OR-INCA to the aging scheme by Liu et al. [2011] and to the aging scheme by Zhang et al. [2015].  $F_M$  is the BC RF estimated by the bottom-up method;  $o/m$  is the ratio of observed and modeled BC AAOD at 900 nm;  $s$  is the scaling factor derived by equation (3) in the Bayesian method; and  $F_B$  is the BC RF estimated by the Bayesian method. Results are shown by region (EA for East Asia, SSA for South and Southeast Asia, ME for Middle East, NA for North America, SA for South America, and OCE for Oceania).

[2011],  $\beta$ [OH] is based on the condensation of sulfuric but implicitly includes the effect of other species related with oxidants (e.g., nitrate acids). In the work by Liu et al. [2011],  $\beta$  was determined by assuming an  $e$ -folding aging time of 2.5 days under globally average [OH], while  $\alpha$  was determined by assuming an  $e$ -folding aging time of 20 days for coagulation. Zhang et al. [2015] tested the aging scheme by Liu et al. [2011] in the Model for OZone and Related chemical Tracers version 4 (MOZART-4) and derived  $\beta$  of  $2.4 \times 10^{-11} \text{ cm}^3 \text{ molecule}^{-1} \text{ s}^{-1}$  and  $\alpha$  of  $1.0 \times 10^{-6} \text{ s}^{-1}$  to achieve a better agreement between model and HIPPO measurements. Note that the scheme by Zhang et al. [2015] predicts a faster aging rate than that by Liu et al. [2011].

We implemented the aging schemes by Liu et al. [2011] and Zhang et al. [2015] in our model and rerun  $E_{PKU}/M_{IN}$  and  $E_{PKU}/M_{INz}$ . The modeled BC AAOD by  $E_{PKU}/M_{INz}$  over Asia with new aging schemes was compared with that with a constant aging rate (Figure 11). We found that a faster aging rate increased the ratio of hydrophilic BC to hydrophobic BC, which increased the light absorption of BC but decreases its lifetime. The scheme by Liu et al. [2011] influenced the BC AAOD slightly, but the scheme by Zhang et al. [2015] significantly increased BC AAOD over regions close to sources and decreased BC AAOD over regions far away from the sources slightly (Figure 11). Due to a similar reason, Ghan et al. [2012] found that different mixing states of BC produce 10% differences in the direct BC RF only over regions close to fossil fuel sources.

We computed the bottom-up BC RF ( $F_M$ ), the ratio of observed and modeled BC AAOD ( $o/m$ ) in  $E_{PKU}/M_{DS}$ , the scaling factor ( $s$ ) in equation (3), and the BC RF by the Bayesian method ( $F_B$ ) under different aging schemes (Table 3). The global  $F_M$  changes by 2% under different aging schemes. Regionally, a faster BC aging rate by Zhang et al. [2015] increased the  $F_M$  over continents while decreasing the  $F_M$  over the oceans. Over the oceanic regions covered by HIPPO campaign, the value of  $o/m$  increased from 0.64 with a constant aging rate to 0.72 with aging scheme by Zhang et al. [2015], indicating a reduced model bias. Similar to  $F_M$ , the aging scheme does not influence the  $F_B$  estimate much: the global mean  $F_B$  changed from  $0.527 \text{ W m}^{-2}$  with a constant aging time scale to  $0.529 \text{ W m}^{-2}$  with aging scheme by Zhang et al. [2015], while the regional  $F_B$  varied by less than 3% (Table 3).

### 5. Comparison With Previous Estimates

Our estimated global mean BC RF was compared with that in the literature [Bond et al., 2013], which was referenced by the Fifth Assessment Report of IPCC (Figure 9). Bond et al. [2013] derived their central estimate by scaling the modeled BC AAOD to agree with the values retrieved at AERONET sites. The major difference in methodology between the work by Bond et al. [2013] and ours is summarized in Table 4. Notably, Bond et al. [2013] used the sparse AERONET sites to constrain the modeled BC AAOD over all oceans, but, in our study, the BC AAOD was constrained by HIPPO measurements over remote oceans and not constrained over the

**Table 4.** Major Difference in Estimating the BC RF and the Uncertainty Between the Study by *Bond et al.* [2013] and the Present Study

	<i>Bond et al.</i> [2013]	The Present Study
Scaling over land	The BC AAOD is scaled by a scaling factors = $o/m$ where $o$ and $m$ is the observed and modeled BC AAOD average over all AERONET sites, respectively.	The BC AAOD is scaled by a scaling factors = $\frac{V^o}{V^o+V^m} + \frac{V^m}{V^o+V^m}$ where $V^o, V^m$ is the observational and model errors, respectively.
Scaling over oceans	The modeled BC RF over the oceans is constrained using AERONET retrievals at limited numbers of sites over oceans.	The BC RF over the remote oceans is constrained using HIPPO measurements and not constrained over the remaining oceans devoid of observations.
AERONET retrievals	The retrieved BC AAOD at 550 nm is used to constrain the model, with the uncertainty due to the impact of organic matter and dust assessed.	The retrieved BC AAOD at 900 nm is used to constrain the model, with the uncertainty due to the impact of dust optical properties and BC density assessed.
Uncertainty in the scaling process	Uncertainties in the scaling process are assessed due to the spatial pattern of BC AAOD, ambiguity in how the scale factor is defined, the limited number of AERONET sites, clear-sky biases in the BC AAOD, and the influence of BC transport from sources to oceanic regions. Notably, the representative error due to a coarse model resolution is not included.	We use an optimal interpolation theory to estimate the optimal scaling factor, $s$ , which is used to constrain the BC AAOD in the model, and its variance $V^s$ is estimated based on the model and observational uncertainties. The representative error due to a coarse model resolution is included.
Host model uncertainty	Host model uncertainty is assessed by combining the uncertainties due to the effect of surface albedo and the choice of radiative transfer code [Boucher et al., 1998].	Host model uncertainty is derived from a new estimate by <i>Stier et al.</i> [2013].
Influence of vertical profiles in AFE	Influence of vertical profiles in AFE is assessed by testing different vertical locations of BC relative to clouds [Zarzycki and Bond, 2010]. It results in a variation of the global BC RF by 15%.	Uncertainty in AFE is derived from <i>Samset et al.</i> [2013] and <i>Hodnebrog et al.</i> [2014].
Combination of uncertainties	The 90% uncertainty in BC RF is derived by combining the 90% uncertainty in BC AAOD and the 50% uncertainty in BC AFE.	The 90% uncertainty in BC RF is derived by combining the 90% uncertainties in all error sources.

remaining oceans. If the BC RF over all oceans was scaled by the six AERONET sites over oceans (red circles in Figure 1b), the estimate of global mean  $F_S$  will increase from 0.68 to 1.36  $W m^{-2}$  in  $E_{MAC}/M_{IN}$  and from 0.54 to 0.83  $W m^{-2}$  in  $E_{PKU}/M_{DS}$  (Figure 9), close to that (0.71  $W m^{-2}$ ) in *Bond et al.* [2013]. In addition to this, the estimate by *Bond et al.* [2013] was obtained by scaling the BC AAOD and RF with the ratios of modeled to retrieved BC AAOD. However, without using the Bayesian approach and high-resolution model, *Bond et al.* [2013] do not account for the representativeness error when using coarse-resolution models and emission inventory, just as " $E_{MAC}/M_{IN}$ ." The uncertainty in BC RF in the  $E_{MAC}/M_{IN}$  model (−88% to +155%) is higher than that (−88% to +79%) in *Bond et al.* [2013], mainly because we accounted for the representativeness error caused by comparing modeled BC AAOD with a point measurement. Note that our Bayesian approach reduces the uncertainty in the bottom-up estimate and does not necessarily result in a lower uncertainty in  $E_{MAC}/M_{IN}$  than that in *Bond et al.* [2013]. As shown in our study, the model resolution and spatial distribution of emissions is a critical factor when comparing the modeled BC AAOD to observations, which changes the scaling factor used by *Bond et al.* [2013]. Consequently, our best estimate of  $F_B$  by  $E_{PKU}/M_{DS}$  is 0.53  $W m^{-2}$  (0.14 to 1.19), 27% lower than that (0.71  $W m^{-2}$ , 0.08 to 1.27 as 90% uncertainty range) by *Bond et al.* [2013].

Recently, *X. Wang et al.* [2014] addressed the impact of aging and the contribution of brown carbon in the GEOS-Chem model. Replacing a constant aging rate with a treatment of BC coating with sulphate reduces the lifetime of BC from 5.1 days to 4.4 days. As a result, they achieved a better agreement with both near-source and remote BC concentrations. However, the modeled AAOD was still underestimated by a factor of 1.4 to 2.8 over different regions when comparing with AERONET retrievals. They obtained a global mean BC RF of 0.21  $W m^{-2}$  using the scaling method by *Bond et al.* [2013]. Their scaled BC RF is lower than our estimate of  $F_S$  (0.54  $W m^{-2}$ ) and  $F_B$  (0.53  $W m^{-2}$ ) in  $E_{PKU}/M_{DS}$ , mainly due to a lower AFE (100  $W m^{-2}$ ) in their model than that (159  $W m^{-2}$ ) used in our study. In addition, their 90% uncertainty range (0.04–0.53  $W m^{-2}$ ) was narrower than ours in  $F_B$  mainly for three reasons. First, they assumed an uncertainty of −50%/+100% for the BC AAOD over oceans. Our study suggests that this uncertainty is larger based on all bottom-up uncertainties (−95%/+270% in  $E_{PKU}/M_{DS}$ ). Second, the representativeness error due to a coarse model resolution ( $2^\circ \times 2.5^\circ$ ) was also not included by *X. Wang et al.* [2014]. At last, *X. Wang et al.* [2014] did not include host model uncertainty in their estimate.

*Cohen and Wang* [2014] applied a Kalman Filter method to constrain BC emissions using BC AAOD from AERONET, rather than a scaling method by *Bond et al.* [2013]. There are three major differences between

**Table 5.** Sensitivity of the BC RF and Its Uncertainty to AERONET Sampling<sup>a</sup>

	Using All AERONET Data			Removing the AERONET Data With Daily AOD Less Than 0.4		
	<i>o/m</i>	$F_B$ ( $W\ m^{-2}$ )	(Uncertainty) in $F_B$ (%)	<i>o/m</i>	$F_B$ ( $W\ m^{-2}$ )	Uncertainty in $F_B$ (%)
EA	0.973	1.139	−76.1%/+76.7%	1.331	1.557	−97.9%/+98.5%
SSA	1.555	1.416	−61.3%/+63.0%	1.838	1.674	−136.4%/+137.2%
Africa	2.516	2.077	−59.5%/+65.5%	3.632	2.998	−58.6%/+65.5%
Europe	1.786	1.003	−53.2%/+55.8%	2.186	1.227	−61.5%/+64.0%
ME	1.512	1.643	−50.0%/+52.4%	1.760	1.913	−49.4%/+52.1%
NA	2.354	0.862	−71.2%/+75.3%	3.060	1.121	−88.9%/+92.6%
SA	1.166	0.633	−72.5%/+73.4%	2.756	1.496	−52.4%/+53.7%
OCE	1.655	0.392	−55.7%/+58.0%	2.134	0.505	−94.4%/+95.9%

<sup>a</sup>This table compares a case using the Level 1.5 data for backfilling the missing AAOD when AOD < 0.4 in the Level 2.0 data, to a case that we do not perform this backfilling. *o/m* is the ratio of retrieved and modeled BC AAOD at 900 nm and  $F_B$  is the BC RF estimated by the Bayesian method. Results are shown by region (EA for East Asia, SSA for South and Southeast Asia, ME for Middle East, NA for North America, SA for South America, and OCE for Oceania).

Cohen and Wang [2014] and our study. First, they used a priori global BC emissions of  $14.4\ Tg\ yr^{-1}$  for the year of 1990 [Wang, 2004] and obtained a top-down estimate of  $17.8 \pm 5.6\ Tg\ yr^{-1}$  for years after 2000. This a priori emission is a factor of 2 higher than most estimates for years after 2000 [Bond et al., 2007, 2013; Dentener et al., 2006; Junker and Liousse, 2008; Lamarque et al., 2010; Granier et al., 2011; Q. Q. Wang et al., 2014] and that used in our study ( $8.9\ Tg\ yr^{-1}$ ). Second, Cohen and Wang [2014] used a model resolution of  $1.8^\circ$  in latitude and  $2.5^\circ$  in longitude, but the impact of the rather coarse resolution was not considered when comparing to point measurements. Our study shows that the coarse resolution of model can lead to a representativeness error, which was taken into account when estimating the BC RF in our Bayesian estimate. Our approach has a thorough estimation of the errors associated with the aerosol “forward” model. We performed a Monte Carlo simulation to assess the uncertainty in the a priori emissions based on uncertainties in BC emission factors, fuel consumption, and technology fractions. We further considered model uncertainties in the chain processes going from the emissions to AAOD of BC. At last, we applied a Bayesian method to estimate the BC AAOD by making the best account of all model, representativeness, and observational uncertainties. It would be interesting to translate the error analysis of Cohen and Wang [2014] into an uncertainty range for the BC RF.

At last, Cohen and Wang [2014] include only stations that have no more than 30% of the AOD under a limit of 0.4. This is motivated by the fact that the uncertainty on the retrieved aerosol South and Southeast Asia (SSA) increases as AOD decreases [Dubovik and King, 2000]. However, this approach eliminates a significant fraction of the AERONET data (there are, e.g., no data left in North America in the nonsummer months) and introduces significant sampling biases when comparing models and observations. We performed a sensitivity test where we removed the AERONET data when the retrieved daily AOD is less than 0.4. The results are shown in Table 5. The agreement between model and observations is less satisfactory when only using AERONET AAOD for daily retrieved AOD larger than 0.4. For instance, the ratio between retrieved and modeled BC AAOD varies from 0.97 to 1.33 in East Asia and from 2.52 to 1.84 in Africa. Meantime, the uncertainty is significantly increased when there is less data coverage over low AOD regions. As an example, the uncertainty for  $F_B$  increases from  $-61.7\%/+63.5\%$  to  $-136.4\%/+137.2\%$  in South and Southeast Asia. As discussed by Bond et al. [2013], the procedure of backfilling the missing AAOD when AOD is less than 0.4 adds noise to the retrieved AAOD, but it reduces the sampling bias. Better models and more studies are needed to improve model-observation comparison methods.

## 6. Conclusions and Implications

In this study, we find that a new emission inventory of BC combined with a high-resolution model could generate a BC field that significantly improves the simulation of BC radiation absorption. A location bias is thus revealed, in that a fraction of AERONET sites are located in the top percentiles of BC AAOD simulated for coarse model grids, which introduces to a representativeness error when comparing the modeled BC AAOD to AERONET observations. It explains partly an underestimation in previous studies. Furthermore, in contrast to previous observational-constrained studies, the uncertainties in models and observations, including the representativeness error, are accounted for estimating the BC RF in a Bayesian method in our study for

the first time. As a result, our observationally constrained estimate of the BC RF is somewhat lower than previous estimates. These results imply that reduction in BC emissions would contribute to slow down global warming, but the contribution is less than previously thought.

However, there is a wide uncertainty range in our Bayesian estimate of BC RF, mainly due to the uncertainty in the AFE of BC, error in the vertical profiles of BC, host model uncertainties, and a limited number of BC AAOD observations in space, especially over the oceans. Further reduction of the uncertainty should be achieved by a better design of the measurement network, further improvements of the emission inventory and model resolution, and better constraints of BC optical properties and vertical profiles over the oceans by observations with an improved treatment of aerosols in the model.

At last, extension of our Bayesian approach presented in this study for estimating other aerosol effects should be done with caution. Our approach is based on the assumption that the relationship is linear between emissions and AAOD and between AAOD and RF. Other approaches should be applied when constraining the indirect or the semidirect effects when the relationship with emissions may be nonlinear.

### Acknowledgments

The authors thank the AERONET investigators for establishing and maintaining the 617 sites used in this study (<http://aeronet.gsfc.nasa.gov/>) and Ether/ECCAD for distribution of emission data used in this study ([http://eccad.pole-ether.fr/eccad\\_extract\\_interface/JSF/page\\_login.jsf](http://eccad.pole-ether.fr/eccad_extract_interface/JSF/page_login.jsf)). The PKU-BC-2007 inventory is available at <http://inventory.pku.edu.cn/home.html>. We thank D. Hauglustaine, Y. Yin, and L. Wu for useful comments and discussions and J. Gash for editing the English. This study was supported by the National Natural Science Foundation of China (41390240 and 41130754), the 111 program (B14001), the Agence Nationale de la Recherche (project: ANR-09-CEP-005-03/PAPRIKA), and the National Aeronautics and Space Administration under grant 09-GLORY09-0028 issued through the Science Mission Directorate. Some of the computations were performed using HPC resources from GENCI-TGCC (grant 2013-t2013012201). R.W., O.B., Y.B., and S.T. designed the research. R.W. performed the analysis and calculation. R.W., O.B., and F.C. designed and performed the data assimilation analysis. G.L.S. performed the AERONET data analysis. M.V. carried out the CHIMERE simulation. B.H. S. performed the sensitivity test of vertical profiles. All authors contributed to the interpretation of the results and writing of the paper.

### References

- Adachi, K., S. H. Chung, and P. R. Buseck (2010), Shapes of soot aerosol particles and implications for their effects on climate, *J. Geophys. Res.*, *115*, D17210, doi:10.1029/2009JD013616.
- Adams, P. J., and J. H. Seinfeld (2002), Predicting global aerosol size distributions in general circulation models, *J. Geophys. Res.*, *107*(D19), 4370, doi:10.1029/2001JD001010.
- Aquila, V., et al. (2011), MADE-in: A new aerosol microphysics submodel for global simulation of insoluble particles and their mixing state, *Geosci. Model Dev.*, *4*, 325–355, doi:10.5194/gmd-4-325-2011.
- Balkanski, Y., G. Myhre, M. Gauss, G. Radel, E. J. Highwood, and K. P. Shine (2010), Direct radiative effect of Aerosol emitted by transport from road, ships and aviation, *Atmos. Chem. Phys.*, *10*, 4477–4489.
- Bauer, S. E., and S. Menon (2012), Aerosol direct, indirect, semidirect, and surface albedo effects from sector contributions based on the IPCC AR5 emissions for preindustrial and present-day conditions, *J. Geophys. Res.*, *117*, D01206, doi:10.1029/2011JD016816.
- Bauer, S. E., S. Menon, D. Koch, T. C. Bond, and K. Tsigaridis (2010), A global modeling study on carbonaceous aerosol microphysical characteristics and radiative effects, *Atmos. Chem. Phys.*, *10*, 7439–7456, doi:10.5194/acp-10-7439-2010.
- Bond, T. C., and R. W. Bergstrom (2006), Light absorption by carbonaceous particles: An investigative review, *Aerosol Sci. Technol.*, *40*, 27–67.
- Bond, T. C., D. G. Streets, K. F. Yarber, S. M. Nelson, J.-H. Woo, and Z. Klimont (2004), A technology-based global inventory of black and organic carbon emissions from combustion, *J. Geophys. Res.*, *109*, D14203, doi:10.1029/2003JD003697.
- Bond, T. C., G. Habib, and R. W. Bergstrom (2006), Limitations in the enhancement of visible light absorption due to mixing state, *J. Geophys. Res.*, *111*, D20211, doi:10.1029/2006JD007315.
- Bond, T. C., E. Bhardwaj, R. Dong, R. Jogani, S. Jung, C. Roden, D. G. Streets, and N. M. Trautmann (2007), Historical emissions of black and organic carbon aerosol from energy-related combustion, 1850–2000, *Global Biogeochem. Cycles*, *21*, GB2018, doi:10.1029/2006GB002840.
- Bond, T. C., et al. (2013), Bounding the role of black carbon in the climate system: A scientific assessment, *J. Geophys. Res. Atmos.*, *118*, 5380–5552, doi:10.1002/jgrd.50171.
- Boucher O. (2015), Physical, chemical and optical aerosol properties, in *Atmospheric Aerosols*, pp. 25–49, Springer, Netherlands, doi:10.1007/978-94-017-9649-1\_3.
- Boucher, O., et al. (1998), Intercomparison of models representing direct shortwave radiative forcing by sulfate aerosols, *J. Geophys. Res.*, *103*(D14), 16,979–16,998, doi:10.1029/98JD00997.
- Boucher, O., et al. (2013), Clouds and Aerosols, in *Climate Change 2013: The Physical Science Basis. Contribution of Working Group I to the Fifth Assessment Report of the Intergovernmental Panel on Climate Change*, edited by T. F. Stocker et al., Cambridge Univ. Press, U. K., and New York.
- Bouttier, F., and P. Courtier (1999), Data assimilation concepts and methods. *ECMWF Meteorological Training Course Lecture Series*, 10–16.
- Chung, C. E., V. Ramanathan, D. Kim, and I. A. Podgorny (2005), Global anthropogenic aerosol direct forcing derived from satellite and ground-based observations, *J. Geophys. Res.*, *110*, D24207, doi:10.1029/2005JD006356.
- Chung, C. E., V. Ramanathan, and D. Decremmer (2012), Observationally constrained estimates of carbonaceous aerosol radiative forcing, *Proc. Natl. Acad. Sci. U. S. A.*, *109*, 11,624–11,629.
- Chung, S. H., and J. H. Seinfeld (2002), Global distribution and climate forcing of carbonaceous aerosols, *J. Geophys. Res.*, *107*(D19), 4407, doi:10.1029/2001JD001397.
- Chylek, P., V. Srivastava, R. G. Pinnick, and R. T. Wang (1988), Scattering of electromagnetic waves by composite spherical particles: Experiment and effective medium approximations, *Appl. Opt.*, *27*(12), 2396–2404.
- Cohen, J. B., and C. Wang (2014), Estimating global black carbon emissions using a top-down Kalman Filter approach, *J. Geophys. Res. Atmos.*, *119*, 307–323, doi:10.1002/2013JD019912.
- Cooke, W. F., and J. J. N. Wilson (1996), A global black carbon aerosol model, *J. Geophys. Res.*, *101*, 19,395–19,409, doi:10.1029/96JD00671.
- Corrigan, C. E., G. C. Roberts, M. V. Ramana, D. Kim, and V. Ramanathan (2008), Capturing vertical profiles of aerosols and black carbon over the Indian Ocean using autonomous unmanned aerial vehicles, *Atmos. Chem. Phys.*, *8*, 737–747.
- Dentener, F., et al. (2006), Emissions of primary aerosol and precursor gases in the years 2000 and 1750 prescribed data-sets for Aerocom, *Atmos. Chem. Phys.*, *6*, 4321–4344.
- Dubovik, O., and M. D. King (2000), A flexible inversion algorithm for retrieval of aerosol optical properties from Sun and sky radiance measurements, *J. Geophys. Res.*, *105*, 20,673–20,696, doi:10.1029/2000JD900282.
- European Centre for Medium-Range Weather Forecasts (2003), Forty-year European reanalysis of the global atmosphere. [Available at <http://www.ecmwf.int/products/>, Accessed on 6 Nov 2013.]
- Engelen, R. J., A. S. Denning, K. R. Gurney, and TransCom3 modelers (2002), On error estimation in atmospheric CO<sub>2</sub> inversions, *J. Geophys. Res.*, *107*(D22), 4635, doi:10.1029/2002JD002195.

- Esteve, A. R., J. A. Ogren, P. J. Sheridan, E. Andrews, B. N. Holben, and M. P. Utrillas (2012), Sources of discrepancy between aerosol optical depth obtained from AERONET and in-situ aircraft profiles, *Atmos. Chem. Phys.*, *12*, 2987–3003.
- Formenti, P., W. Elbert, W. Maenhaut, J. Haywood, S. Osborne, and M. O. Andreae (2003), Inorganic and carbonaceous aerosols during the Southern African Regional Science Initiative (SAFARI 2000) experiment: Chemical characteristics, physical properties, and emission data for smoke from African biomass burning, *J. Geophys. Res.*, *108*(D13), 8488, doi:10.1029/2002JD002408.
- Ghan, S. J., X. Liu, R. C. Easter, R. Zaveri, P. J. Rasch, and J. H. Yoon (2012), Toward a minimal representation of aerosols in climate models: Comparative decomposition of aerosol direct, semidirect, and indirect radiative forcing, *J. Clim.*, *25*, 6461–6476.
- Granier, C., et al. (2011), Evolution of anthropogenic and biomass burning emissions of air pollutants at global and regional scales during the 1980–2010 period, *Clim. Change*, *109*, 163–190.
- Hauglustaine, D. A., Y. Balkanski, and M. Schulz (2014), A global model simulation of present and future nitrate aerosols and their direct radiative forcing of climate, *Atmos. Chem. Phys.*, *14*, 11,031–11,063.
- Hess, M., P. Koepke, and I. Schult (1998), Optical properties of aerosols and clouds: The software package OPAC, *Bull. Am. Meteorol. Soc.*, *79*, 831–844.
- Hodnebrog, Ø., G. Myhre, and B. H. Samset (2014), How shorter black carbon lifetime alters its climate effect, *Nat. Commun.*, *5*, 5065.
- Holben, B., et al. (1998), AERONET—A federated instrument network and data archive for aerosol characterization, *Remote Sens. Environ.*, *66*, 1–16.
- Hourdin, F., et al. (2006), The LMDZ4 general circulation model: Climate performance and sensitivity to parametrized physics with emphasis on tropical convection, *Clim. Dyn.*, *27*, 787–813.
- Jacobson, M. Z. (2001), Strong radiative heating due to the mixing state of black carbon in atmospheric aerosols, *Nature*, *409*, 695–697.
- Jacobson, M. Z. (2010), Short-term effects of controlling fossil-fuel soot, biofuel soot and gases, and methane on climate, Arctic ice, and air pollution health, *J. Geophys. Res.*, *115*, D14209, doi:10.1029/2009JD013795.
- Jacobson, M. Z. (2012), Investigating cloud absorption effects: Global absorption properties of black carbon, tar balls, and soil dust in clouds and aerosols, *J. Geophys. Res.*, *117*, D06205, doi:10.1029/2011JD017218.
- Junker, C., and C. Liou (2008), A global emission inventory of carbonaceous aerosol from historic records of fossil fuel and biofuel consumption for the period 1860–1997, *Atmos. Chem. Phys.*, *8*, 1195–1207.
- Kim, D., C. Wang, A. M. L. Ekman, M. C. Barth, and P. J. Rasch (2008), Distribution and direct radiative forcing of carbonaceous and sulfate aerosols in an interactive size-resolving aerosol-climate model, *J. Geophys. Res.*, *113*, D16309, doi:10.1029/2007JD009756.
- Kim, D., et al. (2011), Dust optical properties over North Africa and the Arabian Peninsula derived from the AERONET dataset, *Atmos. Chem. Phys.*, *11*, 10,733–10,741.
- Kipling, Z., M. Chin, H. Yu, T. F. Eck, A. Sinyuk, A. Smirnov, and B. N. Holben (2013), Constraints on aerosol processes in climate models from vertically-resolved aircraft observations of black carbon, *Atmos. Chem. Phys.*, *13*, 5969–5986.
- Kirchstetter, T. W., T. Novakov, and P. V. Hobbs (2004), Evidence that the spectral dependence of light absorption by aerosols is affected by organic carbon, *J. Geophys. Res.*, *109*, D21208, doi:10.1029/2004JD004999.
- Koch, D. (2001), Transport and direct radiative forcing of carbonaceous and sulfate aerosols in the GISS GCM, *J. Geophys. Res.*, *106*(D17), 20,311–20,332, doi:10.1029/2001JD900038.
- Koch, D., et al. (2009), Evaluation of black carbon estimations in global aerosol models, *Atmos. Chem. Phys.*, *9*, 9001–9026.
- Krinner, G., N. Viovy, N. de Noblet-Ducoudré, J. Ogee, J. Polcher, P. Friedlingstein, P. Ciais, S. Sitch, and I. C. Prentice (2005), A dynamic global vegetation model for studies of the coupled atmosphere-biosphere system, *Global Biogeochem. Cycles*, *19*, GB1015, doi:10.1029/2003GB002199.
- Lamarque, J. F., et al. (2010), Historical (1850–2000) gridded anthropogenic and biomass burning emissions of reactive gases and aerosols: Methodology and application, *Atmos. Chem. Phys.*, *10*, 7017–7039.
- Liu, J., S. Fan, L. W. Horowitz, and H. Levy II (2011), Evaluation of factors controlling long-range transport of black carbon to the Arctic, *J. Geophys. Res.*, *116*, D04307, doi:10.1029/2010JD015145.
- Liu, X., et al. (2012), Toward a minimal representation of aerosols in climate models: Description and evaluation in the Community Atmosphere Model CAM5, *Geosci. Model Dev.*, *5*, 709–739, doi:10.5194/gmd-5-709-2012.
- Lorenç, A. C. (1986), Analysis methods for numerical weather prediction, *Q. J. R. Meteorol. Soc.*, *112*, 1177–1194.
- Matsui, H., M. Koike, Y. Kondo, N. Moteki, J. D. Fast, and R. A. Zaveri (2013), Development and validation of a black carbon mixing state resolved three-dimensional model: Aging processes and radiative impact, *J. Geophys. Res. Atmos.*, *118*, 2304–2326, doi:10.1029/2012JD018446.
- Maxwell Garnett, J. C. (1904), Colours in metal glasses and in metallic films, *Philos. Trans. R. Soc. London*, *203*, 443–445.
- Menut, L., et al. (2013), CHIMERE 2013: A model for regional atmospheric composition modeling, *Geosci. Model Dev.*, *6*, 981–1028.
- Myhre, G., et al. (2013a), Radiative forcing of the direct aerosol effect from AeroCom Phase II simulations, *Atmos. Chem. Phys.*, *13*, 1853–1877.
- Myhre, G., et al. (2013b), Anthropogenic and natural radiative forcing, in *Climate Change 2013: The Physical Science Basis. Contribution of Working Group I to the Fifth Assessment Report of the Intergovernmental Panel on Climate Change*, edited by T. F. Stocker et al., pp. 659–740, Cambridge Univ. Press, U. K., and New York.
- Oshima, N., and M. Koike (2013), Development of a parameterization of black carbon ageing for use in general circulation models, *Geosci. Model Dev.*, *6*, 263–282.
- Oshima, N., M. Koike, Y. Zhang, Y. Kondo, N. Moteki, N. Takegawa, and Y. Miyazaki (2009), Aging of black carbon in out-flow from anthropogenic sources using a mixing state resolved model: Model development and evaluation, *J. Geophys. Res.*, *114*, D06210, doi:10.1029/2008JD010680.
- Ramanathan, V., and G. Carmichael (2008), Global and regional climate changes due to black carbon, *Nat. Geosci.*, *1*, 221–227.
- Reddy, M. S., O. Boucher, N. Bellouin, M. Schulz, Y. Balkanski, J.-L. Dufresne, and M. Pham (2005), Estimates of global multicomponent aerosol optical depth and direct radiative perturbation in the Laboratoire de Météorologie Dynamique general circulation model, *J. Geophys. Res.*, *110*, D10S16, doi:10.1029/2004JD004757.
- Riemer, N., M. West, R. A. Zaveri, and R. C. Easter (2009), Simulating the evolution of soot mixing state with a particle-resolved aerosol model, *J. Geophys. Res.*, *114*, D09202, doi:10.1029/2008JD011073.
- Riemer, N., M. West, R. A. Zaveri, and R. C. Easter (2010), Estimating soot aging time scales with a particle-resolved aerosol model, *J. Aerosol Sci.*, *41*, 143–158.
- Samset, B. H., et al. (2013), Black carbon vertical profiles strongly affect its radiative forcing uncertainty, *Atmos. Chem. Phys.*, *13*, 2423–2434.
- Samset, B. H., et al. (2014), Modelled black carbon radiative forcing and atmospheric lifetime in AeroCom Phase II constrained by aircraft observations, *Atmos. Chem. Phys.*, *14*, 12,465–12,477.
- Sato, M., J. Hansen, D. Koch, A. Lacis, R. Ruedy, O. Dubovik, B. Holben, M. Chin, and T. Novakov (2003), Global atmospheric black carbon inferred from AERONET, *Proc. Natl. Acad. Sci. U.S.A.*, *100*, 6319–6324.
- Schulz, M. (2007), Constraining Model Estimates of the Aerosol Radiative Forcing, Thèse d'Habilitation à Diriger des Recherches, Université Pierre et Marie Curie, Paris VI.
- Schulz, M., Y. J. Balkanski, W. Guelle, and F. Dulac (1998), Role of aerosol size distribution and source location in a three-dimensional simulation of a Saharan dust episode tested against satellite-derived optical thickness, *J. Geophys. Res.*, *103*, 10,579–10,592, doi:10.1029/97JD02779.

- Schulz, M., et al. (2006), Radiative forcing by aerosols as derived from the AeroCom present-day and pre-industrial simulations, *Atmos. Chem. Phys.*, *6*, 5225–5246.
- Schuster, G. L., O. Dubovik, B. N. Holben, and E. E. Clothiaux (2005), Inferring black carbon content and specific absorption from Aerosol Robotic Network (AERONET) aerosol retrievals, *J. Geophys. Res.*, *110*, D10S17, doi:10.1029/2004JD004548.
- Schuster, G. L., B. Lin, and O. Dubovik (2009), Remote sensing of aerosol water uptake, *Geophys. Res. Lett.*, *36*, L03814, doi:10.1029/2008GL036576.
- Schuster, G. L., O. Dubovik, and A. Arola (2016), Remote sensing of soot carbon-Part 1: Distinguishing different absorbing aerosol species, *Atmos. Chem. Phys.*, *16*, 1565–1585.
- Schuster, G., M. Vaughan, D. MacDonnell, W. Su, D. Winker, O. Dubovik, T. Lapyonok, and C. Trepte (2012), Comparison of CALIPSO aerosol optical depth retrievals to AERONET measurements, and a climatology for the lidar ratio of dust, *Atmos. Chem. Phys.*, *12*, 7431–7452.
- Schwarz, J. P., B. H. Samset, A. E. Perring, J. R. Spackman, R. S. Gao, P. Stier, M. Schulz, F. L. Moore, E. A. Ray, and D. W. Fahey (2013), Global-scale seasonally resolved black carbon vertical profiles over the Pacific, *Geophys. Res. Lett.*, *40*, 5542–5547, doi:10.1002/2013GL057775.
- Shindell, D. T., et al. (2008), A multi-model assessment of pollution transport to the Arctic, *Atmos. Chem. Phys.*, *8*, 5353–5372.
- Shindell, D., et al. (2012), Simultaneously mitigating near-term climate change and improving human health and food security, *Science*, *335*, 183–189.
- Spracklen, D. V., et al. (2005), A global off-line model of size-resolved aerosol microphysics: II. Identification of key uncertainties, *Atmos. Chem. Phys.*, *5*, 3233–3250.
- Sreekanth, V., K. Niranjana, and B. L. Madhavan (2007), Radiative forcing of black carbon over eastern India, *Geophys. Res. Lett.*, *34*, L17818, doi:10.1029/2007GL030377.
- Stier, P., et al. (2005), The aerosol-climate model ECHAM5-HAM, *Atmos. Chem. Phys.*, *5*, 1125–1156.
- Stier, P., et al. (2013), Host model uncertainties in aerosol radiative forcing estimates: Results from the AeroCom Prescribed intercomparison study, *Atmos. Chem. Phys.*, *13*, 3245–3270.
- Tang, I. N., and H. R. Munkelwitz (1994), Water activities, densities, and refractive indices of aqueous sulfates and sodium nitrate droplets of atmospheric importance, *J. Geophys. Res.*, *99*(D9), 18,801–18,808, doi:10.1029/94JD01345.
- van der Werf, G. R., J. T. Randerson, L. Giglio, G. J. Collatz, P. S. Kasibhatla, and A. F. Arellano Jr. (2006), Interannual variability in global biomass burning emissions from 1997 to 2004, *Atmos. Chem. Phys.*, *6*, 3423–3441.
- van der Werf, G. R., J. T. Randerson, L. Giglio, G. J. Collatz, M. Mu, P. S. Kasibhatla, D. C. Morton, R. S. DeFries, Y. Jin, and T. T. van Leeuwen (2010), Global fire emissions and the contribution of deforestation, savanna, forest, agricultural, and peat fires (1997–2009), *Atmos. Chem. Phys.*, *10*, 11,707–11,735.
- Wang, C. (2004), A modeling study on the climate impacts of black carbon aerosols, *J. Geophys. Res.*, *109*, D03106, doi:10.1029/2003JD004084.
- Wang, Q. Q., D. J. Jacob, J. R. Spackman, A. E. Perring, J. P. Schwarz, N. Moteki, E. A. Marais, C. Ge, J. Wang, and S. R. H. Barrett (2014), Global budget and radiative forcing of black carbon aerosol: Constraints from pole-to-pole (HIPPO) observations across the Pacific, *J. Geophys. Res. Atmos.*, *119*, 195–206, doi:10.1002/2013JD020824.
- Wang, R., et al. (2012a), Black carbon emissions in China from 1949 to 2050, *Environ. Sci. Technol.*, *46*, 7595–7603.
- Wang, R., et al. (2012b), Global emission of black carbon from motor vehicles from 1960 to 2006, *Environ. Sci. Technol.*, *46*, 1278–1284.
- Wang, R., et al. (2013), High-resolution mapping of combustion processes and implications for CO<sub>2</sub> emissions, *Atmos. Chem. Phys.*, *13*, 5189–5203.
- Wang, R., et al. (2014a), Exposure to ambient black carbon derived from a unique inventory and high-resolution model, *Proc. Natl. Acad. Sci. U.S.A.*, *111*, 2459–2463.
- Wang, R., et al. (2014b), Trend in global black carbon emissions from 1960 to 2007, *Environ. Sci. Technol.*, *48*, 6780–6787.
- Wang, X., C. L. Heald, D. A. Ridley, J. P. Schwarz, J. R. Spackman, A. E. Perring, H. Coe, D. Liu, and A. D. Clarke (2014), Exploiting simultaneous observational constraints on mass and absorption to estimate the global direct radiative forcing of black carbon and brown carbon, *Atmos. Chem. Phys.*, *14*, 10,989–11,010.
- Wilson, J., C. Cuvelier, and F. Raes (2001), A modeling study of global mixed aerosol fields, *J. Geophys. Res.*, *106*, 34,081–34,108, doi:10.1029/2000JD000198.
- Wofsy, S. C. (2012), *HIPPO Merged 10-Second Meteorology, Atmospheric Chemistry, Aerosol Data (R\_20121129)*, Carbon Dioxide Information Analysis Center, Oak Ridge National Laboratory, Oak Ridge, Tenn., doi:10.3334/CDIAC/hippo\_010.
- Wofsy, S. C., HIPPO Science Team, and Cooperating Modellers and Satellite Teams (2011), HIAPER pole-to-pole observations (HIPPO): Fine-grained, global-scale measurements of climatically important atmospheric gases and aerosols, *Philos. Trans. R. Soc. London, Ser. A*, *369*, 2073–2086.
- Zarzycki, C. M., and T. C. Bond (2010), How much can the vertical distribution of black carbon affect its global direct radiative forcing?, *Geophys. Res. Lett.*, *37*, L20807, doi:10.1029/2010GL044555.
- Zhang, J., J. Liu, S. Tao, and G. A. Ban-Weiss (2015), Long-range transport of black carbon to the Pacific Ocean and its dependence on ageing timescale, *Atmos. Chem. Phys.*, *15*, 11,521–11,535.